ARTICLE IN PRESS

Journal of Sound and Vibration ∎ (∎∎∎∎) ∎∎∎–∎∎∎

Contents lists available at SciVerse ScienceDirect

Journal of Sound and Vibration

journal homepage: www.elsevier.com/locate/jsvi

Review

Farfield filtering and source imaging of subsonic jet noise

Maxime Kœnig [a,b,*], André V.G. Cavalieri [a,c], Peter Jordan [a], Joël Delville [a], Yves Gervais [a], Dimitri Papamoschou [d]

[a] Institut Pprime, CNRS – Université de Poitiers – ENSMA, UPR 3346, 43 rue de l'Aérodrome, 86036 Poitiers, France
[b] Snecma (Safran Group), Acoustic Department, Rond Point René Ravaud, 77550 Moissy-Cramayel, France
[c] Instituto Tecnológico de Aeronáutica, Praça Mal. Eduardo Gomes, 50, Vila das Acácias, 12228-900, São José dos Campos, SP, Brazil
[d] University of California Irvine, Irvine, USA

ARTICLE INFO

Article history:
Received 19 March 2012
Received in revised form
19 January 2013
Accepted 22 February 2013
Handling Editor: P. Joseph

ABSTRACT

Jet noise is analysed using data-processing tools adapted to two particular structural traits of the far field: the strong polar dependence and the temporal intermittency. Proper Orthogonal Decomposition is used to probe the polar structure of the sound field, wavelet transform being used to interrogate the temporal signature. The far field is decomposed, using each of these approaches independently, into a component attributed to 'coherent structures', denoted CS, and a residuum, R. The criteria for the decomposition being different, spatial on one hand and temporal on the other, comparison of the resulting CS components is of considerable interest; both decompositions lead, for instance, to CS components that compare favourably with a wavepacket source Ansatz.

Using the two techniques, an analysis methodology is established and applied to data from a Mach 0.9, isothermal jet; a series of metrics are thereby proposed by which to evaluate the data. The methodology and associated metrics are then used to explore the effect of varying Mach number on isothermal and heated jets. The following main results are obtained. Both the unfiltered low-angle sound spectrum and that of the CS component of the isothermal jets are found to scale best with Helmholtz number, indicating that the associated sound source is noncompact. In the heated jet, on the other hand, a Strouhal number scaling is observed, again for both the unfiltered low-angle spectrum and the CS spectrum, suggesting that the associated sources are in this case more compact. Where the intermittency of the farfield signature is concerned it is found that increasing the Mach number of isothermal jets has no discernible impact, whereas in the case of the heated jet this increase is accompanied by a decrease in the intermittency, indicating some kind of associated stabilisation of wavepacket source dynamics. Finally, the unfiltered data is used to perform source imaging, using a wavepacket Ansatz. This allows a more comprehensive eduction of the wavepacket parameters. The trends observed are consistent with known changes in the mean field and with linear stability theory. Finally, the directivity of the wavepackets obtained using the source imaging is compared with those educed from the data using the POD and wavelet filters. Good agreement between all three constitutes a strong evidence supporting the contention that such wavepackets underpin the said, polar and temporal, features of the farfield.

* Corresponding author at: Snecma (Safran Group), Acoustic Department, Rond Point René Ravaud, 77550 Moissy-Cramayel, France. Tel.: +33 160594819.
E-mail address: maxime.koenig@snecma.fr (M. Kœnig).

0022-460X/$ - see front matter © 2013 Elsevier Ltd. All rights reserved.
http://dx.doi.org/10.1016/j.jsvi.2013.02.040

Contents

1. Introduction

Clear phenomenological descriptions of the mechanisms responsible for jet noise remain elusive, despite the presence of a number of clues in the radiated sound field. Two such clues are the angular dependence of the power spectral density of pressure, and the tendential inversion that occurs in heated jets at Mach 0.7: above and below this value heating respectively decreases and increases the radiated sound power [1]. Much of the discussion undertaken by the research community is fueled by these observations.

The peaky spectrum observed at low angles (with respect to the jet axis) in the sound field of jets is frequently attributed to coherent structures, or wavepackets [2]. The more broadband sideline spectrum, on the other hand, is often argued to be associated with ‘fine-scale’ turbulence [3], although it is not clear what ‘fine-scale’ means precisely. In addition, recent work has shown that the sources responsible for sideline radiation may also be modelled as wavepackets with high azimuthal wavenumbers [4].

The dynamic modelling of wavepackets has generally relied on some form of linear stability analysis [5–7], to name a few): the mean velocity field is understood to behave as an equivalent laminar flow which supports large-scale undulations. These undulations take the form of convected wavepackets that amplify and decay as they evolve downstream. The spatially localised character of the wavepackets constitutes a salient feature where low-angle sound production is concerned: such modulation leads to axial imbalances, between regions of positive and negative stress (or pressure), resulting in incomplete cancellation and a consequent unsteady compression and rarefaction of the fluid medium. Viewed in spectral space the same spatial modulation is argued to lead to the appearance of radiation-capable ‘scales’ (those satisfying the dispersion relation $\omega = |\mathbf{k}|c$) [8]. However, this interpretation requires infinitely extended Fourier modes (in both space and time) to be evoked; the problem is then nonlocal and so it is difficult to say precisely where or when sound is produced.

A further characteristic of the sound radiated to low downstream angles, which has been recognised for some time [9–11], and which is now receiving closer attention, in terms of both analysis [12,13] and modelling [14,15], is its temporal intermittency: the most energetic sound-producing events occur in temporally localised bursts. This means that Fourier analysis is poorly adapted for an insight-providing description of both ‘source’ and sound: the projection of the space-time structure of either onto infinitely extended Fourier modes will tend to smear the local details of the sound-production events across a large band of frequencies; the most salient local details may thus be lost.

On account of these two wavepacket characteristics, directivity (a spatial trait) and intermittency (a temporal trait), it makes sense to interrogate the sound field using appropriately adapted data-processing tools. The objective of this paper is to explore jet noise using two such tools, as alternatives to Fourier analysis. The sound field is decomposed, using each of the tools, into a component hypothesised to correspond to ‘coherent structures’, denoted CS, and a residuum, R. The first decomposition is effected using Proper Orthogonal Decomposition (hereafter POD), optimally adapted to the inhomogeneous polar structure of the sound field. In this case the CS component is isolated on account of its directivity. The second decomposition is performed by means of wavelet transforms: each farfield microphone signal is decomposed, independently, into CS and R components, the basis for the decomposition being in this case the aforesaid intermittency. In the approaches followed hereafter, no special consideration is given to the temporal structure of the sound field in the POD decomposition, while the wavelet decomposition disregards the polar structure.

The POD and wavelet CS signatures are compared both with one another and with that of the wavepacket model of Crow [16]. A source imaging technique is then implemented, using the raw data, and this allows a more complete exploration of the wavepacket parameters. The results of the imaging technique are, furthermore, compared with the CS signatures educed using the POD and wavelet filters. Close agreement of all three constitutes strong evidence for the existence of wavepackets whose salient features are their axial noncompactness and their 'jittery' temporal dynamics.

The filtering techniques discussed above are then used to explore the effect of varying the Mach number of isothermal and heated jets. The analysis provides insights regarding the effect of Mach number and temperature on wavepacket sound generation in turbulent jets. Two noteworthy results are: (1) the change in velocity scaling of the CS spectra when the jets are heated: while Helmholtz scaling is observed in the isothermal jets, suggesting that noncompact effects are important, the CS spectra of the heated jet scale best with Strouhal number, suggesting that the underlying sources are more compact; (2) while the intermittency of the sound field radiated by the isothermal jets is not affected by Mach number, in the case of the heated flow increasing the Mach number leads to a *decrease* in the observed intermittency, suggesting some associated stabilising effect where the source dynamics are concerned.

The paper is organised as follows. After a brief description of the experiment and the database in Section 2, a detailed exposition of the analysis tools is provided in Section 3. This exposition involves an application to data from an isothermal, Mach 0.9 jet. Metrics and an associated analysis methodology are established using this data, and these are subsequently applied, in Sections 4 and 5, to explore the Mach number effect in isothermal and heated jets. Finally, in Section 6, a source imaging technique is applied to the unfiltered data, from both the isothermal and heated jets, and the results are compared with those obtained using the POD and wavelet filters.

2. Experiment

The experiments were carried out at the MARTEL facility of the Pprime Institute, CEAT (Centre d'Études Aérodynamiques et Thermiques), Poitiers, France and are documented by Jordan & Gervais [17]. The jet exit diameter was $D=0.05$ m. The test matrix is shown in Table 1.

In the table, T_j is the jet temperature, T_∞ the ambient temperature, M_a the acoustic Mach number, M_j the jet Mach number and $Re_D = U_j D/\nu$ the jet Reynolds number.

The acoustic field was sampled using an arc of 12 microphones at a distance of 30 diameters from, and centered on, the jet exit. The angular position θ of the microphones varied equispaced from 30° to 140° with respect to the downstream jet axis. The acoustic setup is shown in Fig. 1. Further details regarding the experiments can be found in Jordan and Gervais [17].

Table 1
Test matrix.

Case number	T_j/T_∞	M_a	M_j	Re_D
1	1.0	0.60	0.600	6.7×10^5
2	1.0	0.75	0.750	8.4×10^5
3	1.0	0.90	0.900	1.0×10^6
4	2.0	0.75	0.530	5.1×10^5
5	2.0	0.90	0.636	6.1×10^5
6	2.0	1.00	0.707	6.8×10^5

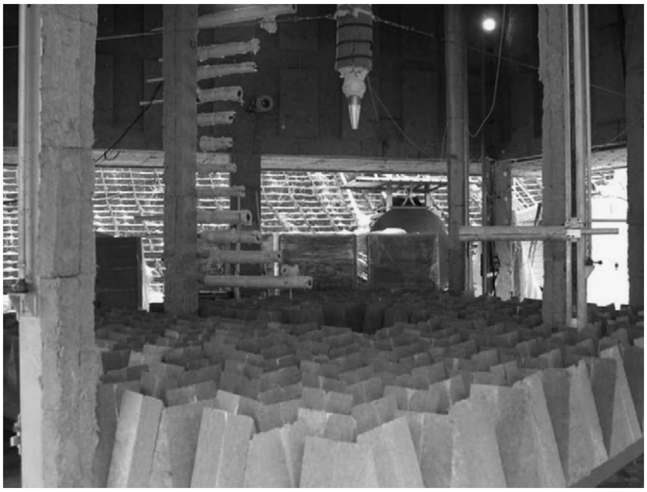

Fig. 1. Acoustic measurement setup.

Please cite this article as: M. Kœnig, et al., Farfield filtering and source imaging of subsonic jet noise, *Journal of Sound and Vibration* (2013), http://dx.doi.org/10.1016/j.jsv.2013.02.040

3. Analysis procedure—applied to jet case 3 ($T_j/T_a = 1; M_a = 0.9$).

The objective of this section is twofold. The filtering operations discussed in the introduction are described via application to the data from the isothermal, Mach 0.9 jet. Metrics and an associated analysis procedure are thereby established for later use in probing the effect of Mach number on sound radiation from isothermal and heated configurations.

Section 3.1 describes how Proper Orthogonal Decomposition is used to explore the polar structure of the sound field. The wavelet filtering and related metrics are presented and discussed in Section 3.2.

3.1. Proper orthogonal decomposition

In the case of farfield jet noise, temporal POD (whose Kernel is a spatial correlation at zero time-delay $\langle p(\theta_i,\tau_i)p(\theta_j,\tau_j=\tau_i)\rangle$) is of limited use, because the microphone signals are more or less de-correlated at zero time delay. The cross-correlation matrix is therefore diagonal, the corresponding eigenfunctions resemble Dirac functions (each with a peak at a given microphone location), and the spectra of the expansion coefficients correspond, approximately, to the microphone spectra. Spectral POD is therefore used to decompose the sound field. In this case the kernel of the POD problem is the cross-spectral matrix $G(\theta_i,\theta_j,\omega)$:

$$G_{ij}(\theta_i,\theta_j,\omega) = \langle \hat{p}(\theta_i,\omega)\hat{p}^*(\theta_j,\omega)\rangle, \tag{1}$$

where $\langle . \rangle$ denotes ensemble averaging, and the following Fredholm integral equation is then solved:

$$\int_D G_{ij}(\theta_i,\theta_j,\omega)\Phi_j^{(n)}(\theta_j,\omega)\,\mathrm{d}\theta_j = \lambda^{(n)}(\omega)\Phi_i^{(n)}(\theta_i,\omega), \tag{2}$$

where λ and Φ_i the eigenvalues and eigenfunctions of the POD problem. Discretisation of the Fredholm integral using the midpoint rule leads to a discrete form of the integral equation, which can be solved using standard matrix eigenvalue routines. The calculation is made one frequency at a time, providing frequency-dependent eigenvalues and eigenvectors. The spatial phase of the soundfield is captured at each frequency, and this information is contained in the shapes of the eigenfunctions (which are complex). The temporal phase is lost, but it can be recovered later by projecting the original data onto the eigenfunctions. Other examples of the use of spectral POD can be found in the work of Delville et al. [18] and Tinney and Jordan [19].

The frequency dependent eigenvalues are shown in Fig. 2(a). It can be seen that the first eigenmode captures a large portion of the energy, particularly at the peak frequency, and has a 'peaky' spectral shape. The higher-order modes are more broadband. The directivity of the modes is shown in Fig. 2(b). Mode 1 clearly dominates the downstream radiation, and has a shape characteristic of a wave-packet type source (more detailed comparisons are made later). The remaining modes have gradually changing spectral shapes and directivity patterns. This decomposition certainly appears to isolate an important dominant source mechanism with spectrum and directivity of the form of the first POD mode; however, there is no clear second mode that might correspond to something which could be associated with a second, statistically independent 'source' mechanism.

Pressure can be recovered thanks to eigenfunctions Φ_i:

$$\hat{p}(\theta_i,\omega) = \sum_{n=1}^{n_{\text{mic}}} a^{(n)}(\omega)\Phi_i^{(n)}(\theta_i,\omega), \tag{3}$$

where n_{mic} is the number of microphones and $a^{(n)}$ are the projection coefficients calculated by

$$a^{(n)}(\omega) = \int_D \hat{p}(\theta_i,\omega)\Phi_i^{*(n)}(\theta_i,\omega)\,\mathrm{d}\theta_i. \tag{4}$$

The first POD mode is retained as the CS component, the remaining modes being lumped together to form the residuum, R. The result in terms of directivity is given in Fig. 2(c). The temporal pressure is obtained by an inverse Fourier transform of $\hat{p}$ calculated by Eq. (3):

$$p_{CS}(\theta,t) = p(\theta,t)^{(1)} \quad \text{and} \quad p_R(\theta,t) = \sum_{n=2}^{n_{\text{mic}}} p(\theta,t)^{(n)}. \tag{5}$$

Fig. 2(d) shows comparison of the directivity with that predicted by the wavepacket source model of Crow [16] (see also Crighton [20] or Ffowcs Williams and Kempton [21]) which takes the form

$$T_{11}(\mathbf{y},\tau) = 2\rho_0 U u' \frac{\pi D^2}{4}\delta(y_2)\delta(y_3)\mathrm{e}^{\mathrm{i}(\omega\tau - k y_1)}\mathrm{e}^{-y_1^2/L^2}, \tag{6}$$

where U is the jet velocity, u' the velocity fluctuations level, $\mathbf{y}$ the observer position, T_{11} the linear component of the axially aligned longitudinal quadrupole distribution of Lighthill, modelled as a convected wave with frequency ω, wavenumber k and which is modulated by a Gaussian axial envelope function. By introducing M_c the Mach number based on the phase velocity U_c (which we assume in this study as $U_c = 0.6U_j$) of the convected wave. Such a source generates a sound field of the

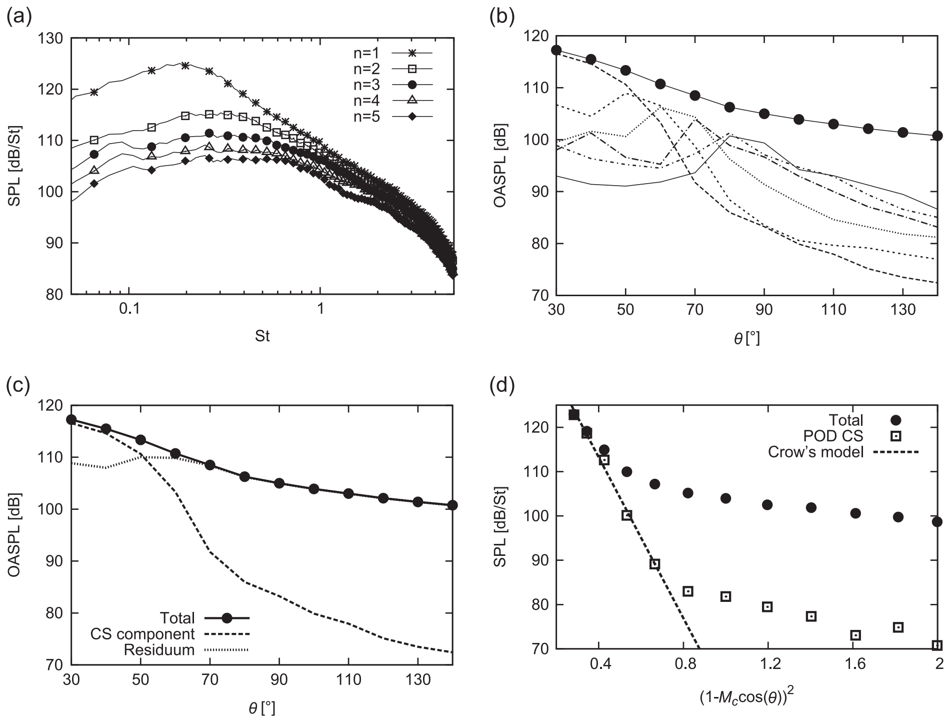

Fig. 2. (a) Eigenspectra, $\lambda^{(n)}(\omega)$ for first five n values (higher n follow the same tendency), (b) OASPL (total and per mode); black dots = baseline OASPL; solid line = sum of POD modes; lines at 30° from top to bottom = contribution of each POD mode (from 1 to 6), (c) contribution of CS and R to OASPL and (d) comparisons between SPL at St=0.2 (total and CS component) and the directivity predicted by Crow's Model. All results are obtained from jet case 3.

form [16]

$$p(\mathbf{x},t) = -\frac{\rho_0 U \tilde{u} M_c^2 (kD^2) L\sqrt{\pi}\cos^2\theta}{8|\mathbf{x}|} \mathrm{e}^{-L^2k^2(1-M_c\cos\theta)^2/4} \mathrm{e}^{\mathrm{i}\omega(t-|\mathbf{x}|/c)}. \tag{7}$$

The sound intensity decays exponentially with $(1-M_c\cos\theta)^2$, a behaviour described as *superdirective* [22]. This expression is for an axisymmetric source, and the justification for its use in the comparisons performed throughout the paper is that the downstream radiation of turbulent jets is predominantly axisymmetric [23,24].

3.2. Wavelet transform

Intermittent acoustic wavepackets will be broken up, de-localised and spread across a range of scales by a Fourier transform. The wavelet transform constitutes a useful tool for the extraction of such time-local signatures. The wavelet transform and some of its properties are here briefly presented. For a more complete exposition the reader can refer to Farge [25]. The continuous wavelet transform of a time pressure signal $p(t)$ is

$$\tilde{p}(s,t) = \int_{-\infty}^{\infty} p(\tau)\psi(s,t-\tau)\,\mathrm{d}\tau, \tag{8}$$

where s is the scale of the wavelet function. A Paul wavelet, which is complex-valued, is used in this study, defined for $s=1$ with an order m as (see [25] for more details):

$$\psi(1,t-\tau) = \frac{2^m \mathrm{i}^m m!}{\sqrt{\pi(2m)!}}[1-\mathrm{i}(t-\tau)]^{-(m+1)}. \tag{9}$$

The motivation for using a complex wavelet is that it better preserves the integrity of individual wavepackets, since the real and imaginary parts of the wavelet allow both high energy peaks and zero crossings associated with a given signature to contribute continually over an integral scale during which the wavepacket is active. Real wavelets will tend to break such single events into unphysical sub-events. These points, addressed more fully in Appendix A, lead us to use the Paul wavelet (whose shape, for $m=4$, is shown in Fig. 3). Further to the property by which this wavelet captures both high amplitudes and high slopes, this particular wavelet comprises shapes that can be observed in the sound pressure signatures of free shear flows (see [9–12])—it is thus useful for feature extraction for our particular physical problem. We nonetheless verify (see Appendix B) that the main results of our analysis are independent of the choice of wavelet family.

Please cite this article as: M. Kœnig, et al., Farfield filtering and source imaging of subsonic jet noise, *Journal of Sound and Vibration* (2013), http://dx.doi.org/10.1016/j.jsv.2013.02.040

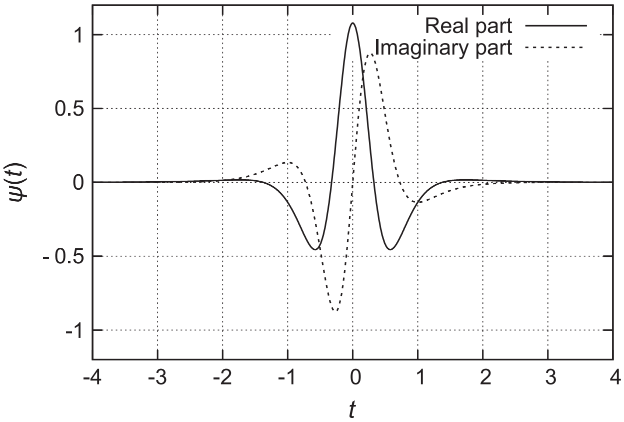

Fig. 3. Paul's wavelet; — real part; - - - imaginary part.

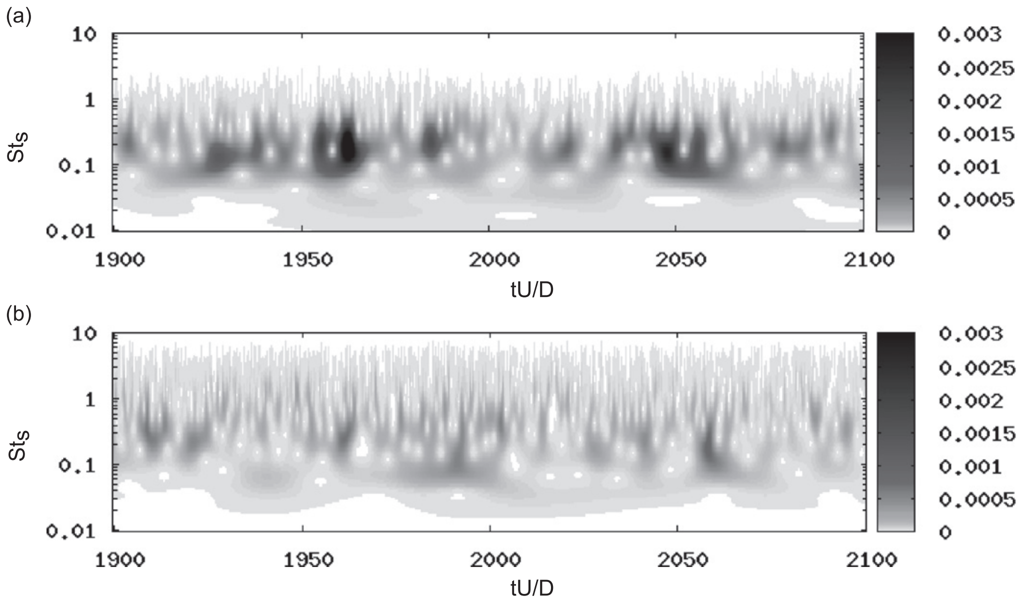

Fig. 4. Wavelet scalogram $|\tilde{p}(s,t)|^2$ at (a) 30°; (b) 90°.

207 scales s are used, defined as fractional powers of two [26]:

$$s_j = s_0 2^{j\delta_j}, \quad j = 0,1,\ldots,J \tag{10}$$

s_0 being the smallest resolvable scale and J the largest scale, so as to cover Strouhal numbers from 0.01 to 10. The scale s is converted to a pseudo-frequency f as in Torrence and Compo [26] (which is then converted to a pseudo-Strouhal number):

$$f_s = (2m+1)/4\pi s \tag{11}$$

$$St_s = f_s D/U_j. \tag{12}$$

The convolution product between pressure signal and wavelet in Eq. (8) is performed in Fourier space, where it amounts to a multiplication. Scalograms of pressure signals, which are the square value of the wavelet transform of the time-domain pressure signal, measured at 30° and 90° for the Mach 0.90 isothermal jet, are shown in Fig. 4. For clarity, only a short time interval (200 convective time scales) of the signal is shown (the original signal has a length of more than 60,000 convective time scales, and filtering is performed over the entire duration of the measurement). Before performing the wavelet transform, the signals are normalised by the RMS pressure at each angle so as to have unit energy regardless of the observation angle.

The 30° scalogram shows bursts of high-amplitude, temporally localised activity, identified by the darker shaded areas (see for example the spots at $tU/D = 1965$ and $tU/D = 2050$). This is the signature of intermittent source activity associated with low-angle radiation. The 90° scalogram, on the other hand, does not have such marked intermittent activity (the scalograms levels are directly comparable on account of the normalisation which has been effected). This difference between low- and high-angle sound radiation constitutes a complementary piece of information – one which is necessarily missed by Fourier analysis – regarding the source dynamics that underpin the well-known directivity and spectral shapes (highlighted in the previous studies by Lush [27], Tanna [1], Viswanathan [28] among others). If this behaviour amounts to an essential aspect of source mechanisms in jets, it needs to be explicitly modelled. Some work in this direction is reported by Sandham et al. [14] and Cavalieri et al. [15].

Intermittency and fluctuation energy. Total energy is conserved under the wavelet transform and there exists the following equivalent of Parseval's theorem [26] for a given pressure signal localised at the angle θ:

$$E = \int_{\mathbb{R}} \left| p(\theta,t) \right|^2 \,\mathrm{d}t = C_\psi^{-1} \int_{\mathbb{R}^+} \int_{\mathbb{R}} \left| \tilde{p}(\theta,s,t) \right| \cdot \left| \tilde{p}^*(\theta,s,t) \right| \frac{\mathrm{d}s\,\mathrm{d}t}{s^2} \tag{13}$$

where $p(\theta,t)$ is the time pressure signal for a given polar position θ, $\tilde{p}(\theta,s,t)$ its continuous wavelet transform and C_ψ is a constant associated with the wavelet function which we use.

The global wavelet spectrum is defined as

$$e_{\text{global}}(\theta,s) = \int_{\mathbb{R}} e(\theta,s,t)\,\mathrm{d}t. \tag{14}$$

It can also be expressed in terms of the Fourier energy spectrum $E(\theta,f) = |\hat{p}(\theta,f)|^2$:

$$e_{\text{global}}(\theta,s) = \int_{\mathbb{R}} E(\theta,f) |\hat{\psi}(sf)|^2 \,\mathrm{d}f, \tag{15}$$

where $\hat{\psi}(sf)$ is the Fourier transform of the wavelet: the global wavelet energy spectrum corresponds to the Fourier energy spectrum smoothed by the wavelet spectrum at each scale. It is then possible to recover the total energy of the field $p(t)$:

$$E(\theta) = C_\psi^{-1} \int_{\mathbb{R}^{+*}} e_{\text{global}}(\theta,s) \frac{\mathrm{d}s}{s}. \tag{16}$$

A threshold parameter, α, is now introduced in order to partition the total energy of the signals considered by means of the following filtering operation:

$$\tilde{p}_f(\alpha,\theta,s,t) = \begin{cases} \tilde{p}(\theta,s,t) & \text{if } |\tilde{p}(\theta,s,t)|^2 > \alpha \\ 0 & \text{if } |\tilde{p}(\theta,s,t)|^2 < \alpha \end{cases}. \tag{17}$$

The parameter α has units of energy density in the wavelet domain. For a given value of the threshold, more energy will be retained by the filtering operation for a peaky scalogram than for a more homogeneous one, and the relationship between the total filtered energy and the threshold energy constitutes a quantitative measure of how peaky the scalogram is.

The following filtering procedure is implemented.

- Perform the wavelet transform on time series from microphones at different angular positions,
- Filter the data in the wavelet domain, using the criterion described above, to obtain $|\tilde{p}(\theta,s,t)|^2$,
- Perform an inverse wavelet transform on the filtered data to obtain filtered temporal pressure signals.

Fig. 5 gives a sense of the difference between this kind of filtering and that which can be obtained in spectral space. A band-pass filter centered on $St{=}0.2$ (which corresponds to the maximum amplitude of the spectrum considered) is

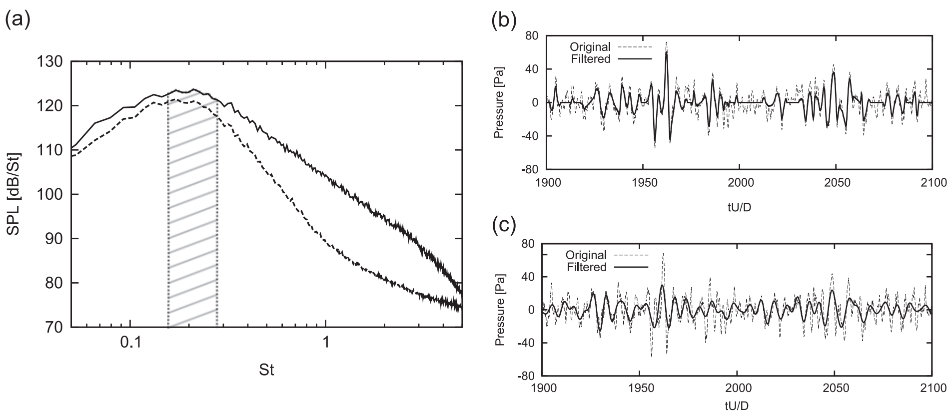

Fig. 5. (a) Comparison of Fourier- and wavelet-based filtering for retention of similar energy; solid line: baseline spectrum; dashed line: wavelet-filtered spectrum; vertical dash-dot line: band-pass Fourier filter; hatche region: energy retained by band-pass filter. Left: Comparison of time-histories of filtered signals; (b) wavelet-filtered and (c) band-pass filtered.

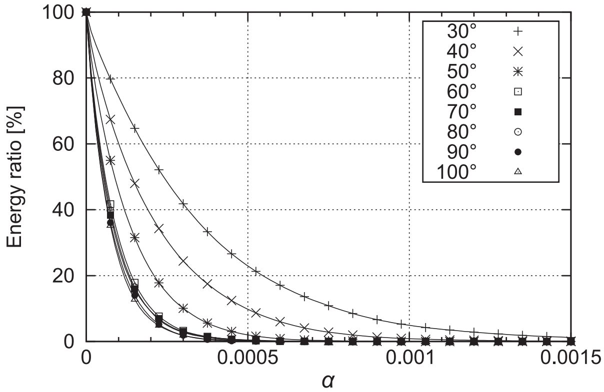

Fig. 6. Energy ratio (filtered/residuum) as a function of polar angle after GIM filtering.

compared with a wavelet-based filter that retains the same energy (around 60 percent at 30°). The time histories best illustrate the differences: the wavelet filter does a better job of retaining the integrity of temporally localised high-amplitude wavepackets, for example at $tU/D = 1960$; whereas the band-pass filter spreads the structure of these more homogeneously over the time-axis.

The percentage of energy retained relative to the total energy of the signal after filtering is assessed as a function of the threshold α:

$$R(\alpha,\theta) = \frac{E_{\text{filtered}}(\alpha,\theta)}{E(\theta)} = \frac{\int_{\mathbb{R}^+}\int_{\mathbb{R}} |\tilde{p}_f(\alpha,\theta,s,t)| \cdot |\tilde{p}_f^*(\alpha,\theta,s,t)| \, \mathrm{d}s \, \mathrm{d}t/s^2}{\int_{\mathbb{R}^+}\int_{\mathbb{R}} |\tilde{p}(\theta,s,t)| \cdot |\tilde{p}^*(\theta,s,t)| \, \mathrm{d}s \, \mathrm{d}t/s^2}. \tag{18}$$

α-dependence of filtered data. A plot of $R(\alpha)$ for the Mach 0.9 cold jet is shown in Fig. 6 for each of the microphones. The curves comprise 100 values of α.

The shape of the curves shown in Fig. 6 amounts to a metric associated with the 'peakiness' of the scalograms; this peakiness is related to the extent to which the amplitudes of the most energetic fluctuations attain extreme values with respect to the signal variance. It can be seen how the signals recorded in the angular range $60° \le \theta \le 100°$ comprise one family of curves. It is possible to conclude that these signals are characterised by similarly low levels of energetic intermittent events. In the angular range $30° \le \theta \le 50°$, on the other hand, we see a gradual evolution from high levels of intermittency at 30° to lower levels similar to those of the low-energy family. These curves will be used in what follows as a metric by which to explore the effect of Mach number on the noise radiated by heated and isothermal jets.

Obtaining CS and R. As there is no a priori objective criterion by which to choose the filter threshold, this becomes a parameter of the study, and, as seen above, the α-dependence of the filtering results is in itself a useful metric by which to evaluate the data. However, an a posteriori criterion is observed on examination of the α-dependence of the spectra of the filtered data: Fig. 7(a) reveals that a peaky asymptotic spectral shape exists at $\alpha = 0.00015$. This threshold value is thus chosen for decomposition of the data into CS component and residuum. Fig. 7(b) shows the scalogram of the CS component. The directivity pattern of the CS component is shown in Fig. 7(c), and in Fig. 7(d) it is compared with the POD CS component and the directivity factor of Crow's wavepacket model.

4. Mach number effect for an isothermal jet

The analysis methodology outlined above is here used to explore the effect of Mach number on isothermal jets, and, in particular, to assess changes in the CS component, as identified by means of both POD and wavelet filtering. In addition to this, the Mach-number dependence of the spectral shapes of both the unfiltered and filtered signals is assessed by plotting the spectra as a function of both Strouhal number and Helmholtz number.

4.1. Spectra and directivity of unfiltered signals

The spectra have been scaled by setting their respective maxima to 0 dB (no shift in frequency is effected). Fig. 8 presents the results of the scaling at 30° as a function of (a) the Helmholtz number (defined as $He = fD/c_\infty$) and (b) the Strouhal number (defined as $St = fD/U$). Best collapse is obtained when scaled using the Helmholtz number (similar observations were made by Lush [27] and Tanna [1]), an indication that source radiation to shallow polar angles is associated with a noncompact source (see Cavalieri et al. [24] for further discussion). Note that at low frequency the Helmholtz scaling is not so good. This is because at low frequency acoustic wavelengths are several jet diameters in length. In such cases, sources can be considered compact, in which case Strouhal scaling is better.

Fig. 9 presents the directivity for different Mach numbers in term of OASPL and SPL at St=0.2, where the level at $\theta = 30°$ is taken as a reference for the dB scale. The directivity is more pronounced at higher Mach numbers, especially when the

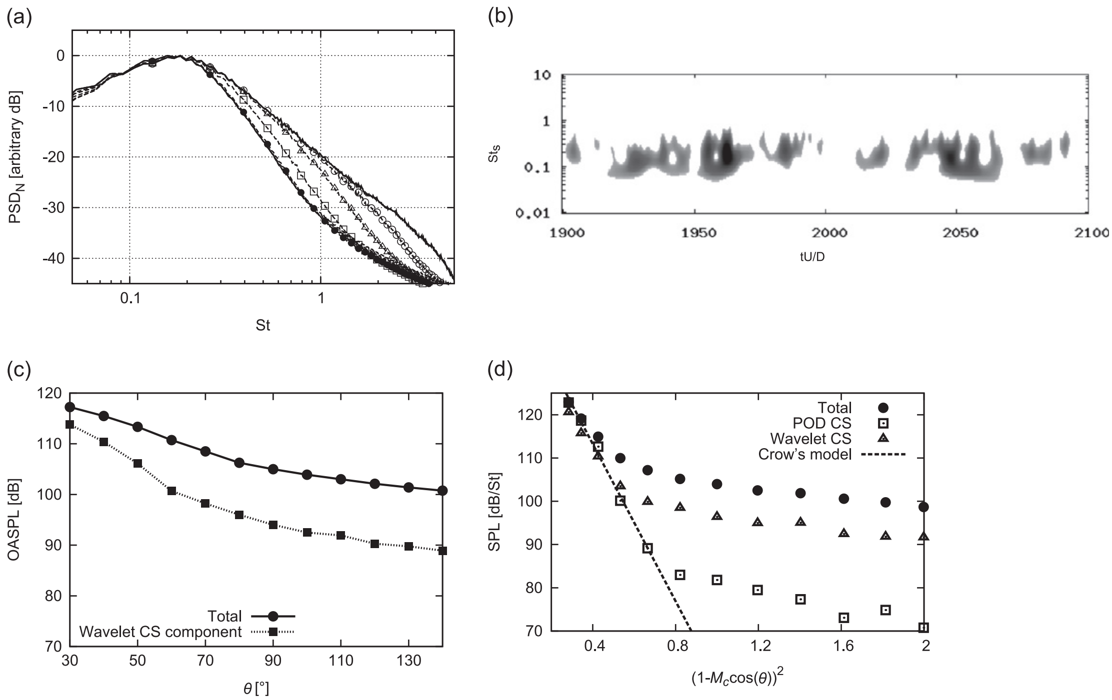

Fig. 7. (a) Normalised autospectra of baseline (—) and filtered component (- - -) at 30° for different filtering threshold α (specific values: -○- 0.00003; -▵- 0.00006; -□- 0.00009; -•- 0.00015; - - - values higher than 0.0015). (b) Wavelet scalogram $|\tilde{p}(s,t)|^2$ at 30° filtered by a $\alpha = 0.00015$ threshold (see Fig. 4 for colour scale). (c) OASPL directivities for total and filtered component ($\alpha = 0.00015$) and (d) comparisons between SPL at $St = 0.2$ (total, POD CS and Wavelet CS) and the directivity predicted by Crow's model.

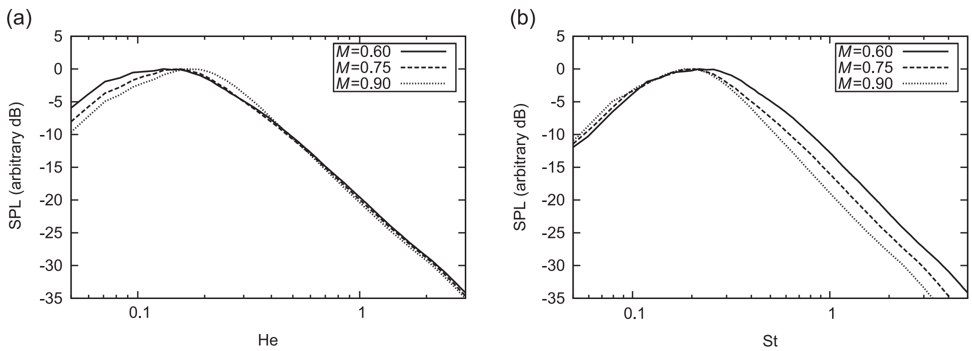

Fig. 8. Spectral shapes for isothermal jets at different Mach numbers, scaled with (a) Helmholtz and (b) Strouhal numbers at $\theta = 30°$.

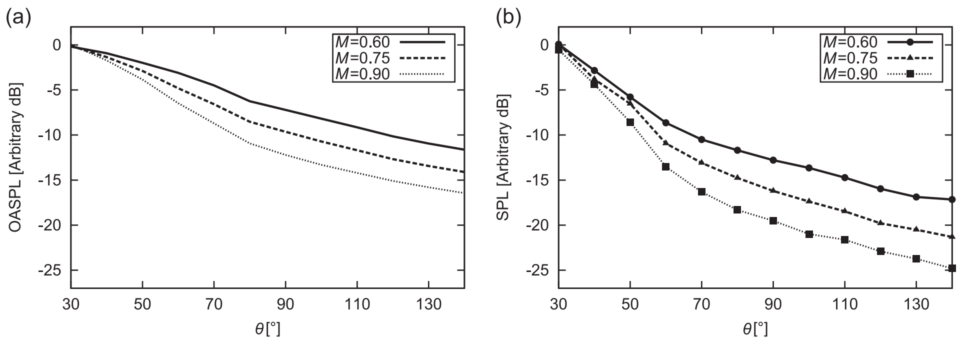

Fig. 9. Directivity for different Mach numbers: (a) OASPL; (b) SPL at $St = 0.2$.

Please cite this article as: M. Kœnig, et al., Farfield filtering and source imaging of subsonic jet noise, *Journal of Sound and Vibration* (2013), http://dx.doi.org/10.1016/j.jsv.2013.02.040

spectral peaks, at $St=0.2$, are considered. In this case, we have a rapid falloff of SPL in the range $30^\circ < \theta < 60^\circ$. The most pronounced directivity is observed at Mach 0.9 where a decrease of more than 13 dB is observed between the SPL at 30° and 60°.

4.2. POD filter

The CS component is obtained using the POD filter as outlined in Section 3. The filtered CS spectra have been scaled for the three Mach numbers 0.60, 0.75 and 0.90, as in Section Appendix A, by both Helmholtz and Strouhal numbers. Fig. 10(a) and (b) compares the spectral shapes at 30°.

As in the baseline case, the spectra scale best with Helmholtz number. We can conclude that the POD filter preserves the noncompact character of the low-angle sound signature.

Fig. 11(a) and (b) show the Mach number dependence of the directivity in terms of OASPL and SPL at $St=0.2$, for both the unfiltered data and the CS components. Comparison of the CS SPL at $St=0.2$ with that of Crow's model, in Fig. 11(c–e), show that the CS component can be considered superdirective, supporting the contention that it is associated with a wavepacket source. Finally, the directivities of the $St=0.2$ SPL are compared for the three Mach numbers in Fig. 12 show how the CS component shows the following trend: as the Mach number increases the slope increases slightly, indicating that the value of kL increases. This means that the wavepacket source at higher Mach number contains more spatial oscillations within the wavepacket envelope. Further discussion on the wavepacket superdirectivity can be found in Cavalieri et al. [24]

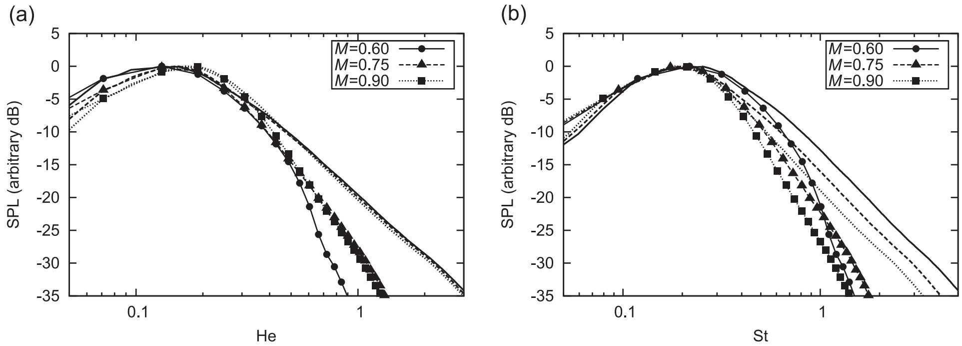

Fig. 10. Spectral shapes at $\theta=30^\circ$ for POD CS component of sound field of isothermal jets at different Mach numbers. (a) Spectra scaled by Helmholtz number; (b) spectra scaled by Strouhal number. Lines without symbols show unfiltered spectra and lines with symbols refer to results of the POD CS component.

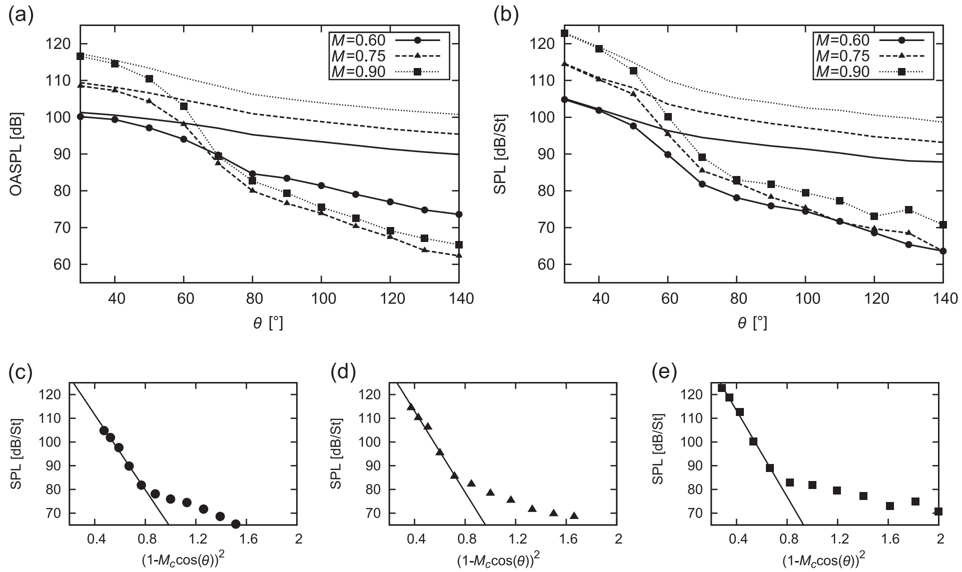

Fig. 11. Directivities for POD CS component of sound field of isothermal jets at different Mach numbers. (a) Comparison of OASPL of total sound field (lines) and CS component (lines with symbols); (b) comparison of SPL, for $St=0.2$, of total sound field and CS component. Superdirectivity of the CS component for (c) Mach 0.60, (d) Mach 0.75 and (e) Mach 0.90.

Please cite this article as: M. Kœnig, et al., Farfield filtering and source imaging of subsonic jet noise, *Journal of Sound and Vibration* (2013), http://dx.doi.org/10.1016/j.jsv.2013.02.040

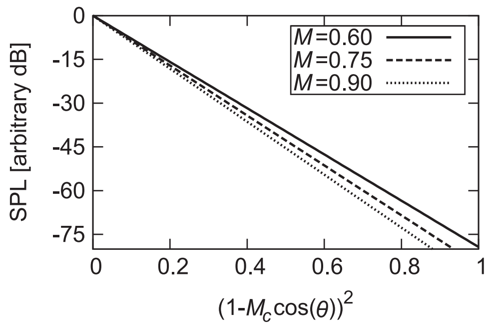

Fig. 12. Comparison of the POD CS component superdirectivities for the three different Mach numbers.

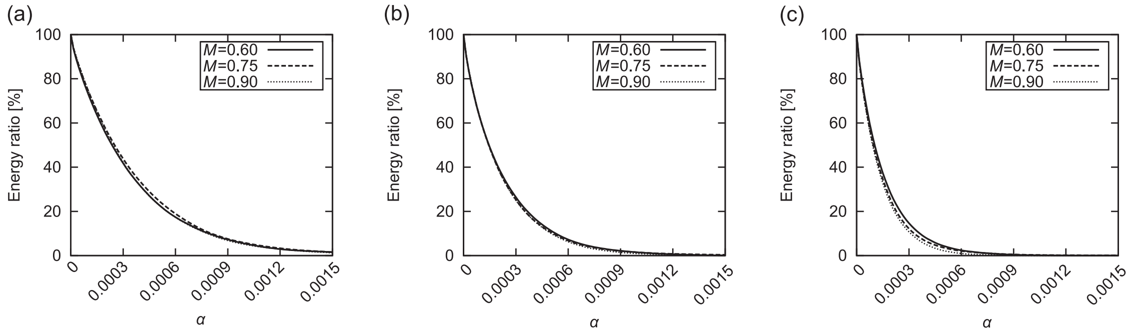

Fig. 13. Energy ratio (filtered/residuum) as a function of Mach number; (a) 30°; (b) 40°; (c) 50°.

4.3. Wavelet filter

The wavelet transform and filtering is performed as presented in Section 3.2. Recall that the analysis comprises two steps: first the filter threshold is varied and the ratio of energy conserved to total energy examined as a function the threshold value (by applying Eq. (18)); then a single threshold value is used, $\alpha = 0.00015$ (which retains of the order of 60 percent of the signal energy at 30°), because it corresponds to a filtering that leads to an asymptotic, 'peaky', spectral shape, in order to effect the decomposition into CS and R components.

The result of varying the threshold is shown in Fig. 13. The shapes of these curves can be considered as a measure of the signal 'burstiness' or intermittency: a curve that decays rapidly with increasing α contains fewer temporally localised events making significant contributions to the overall energy, whereas a curve that decays more slowly with α indicates a greater contribution to the overall energy from such temporally localised events.

The effect of Mach number on this intermittency metric is shown in Fig. 13 for three emission angles, 30°, 40° and 50°. It is possible to conclude that the Mach number does not significantly modify the intermittency of the sound field when the jet remains isothermal. We will see that *this is not the case when the jet is heated.*

The filtered CS spectra at 30° are shown in Fig. 14(a) and (b), plotted as a function of both Strouhal and Helmholtz number. As was the case with the POD CS component, the Helmholtz scaling is preserved by the wavelet filtering.

The OASPL and SPL directivities of the unfiltered and the wavelet-CS component are plotted in Fig. 15(a) and (b) for different Mach numbers. Both are clearly more directive than the baseline case. Comparison with Crow's wavepacket model shows again how the wavelet CS component is superdirective. The Mach number effect on the wavelet CS signature is the same as that observed for the POD CS component: higher Mach number leads to stronger directivity, consistent with a wavepacket source with slightly more spatial oscillations within the envelope. Recall, once again, that the filtering criteria are quite different: the POD appeals to the spatial structure, the wavelet to the temporal intermittency. The fact that both filtering operations produce similar results, consistent with a wavepacket source Ansatz is an indication the spatial and temporal criteria imposed by the filters correspond to salient CS source features.

5. Mach number effect for a heated jet

The analysis is here repeated for a heated jet with temperature ratio equals to 2.0 and an acoustic Mach number varying from 0.75 to 1.00 (cases 4–6) (Fig. 16).

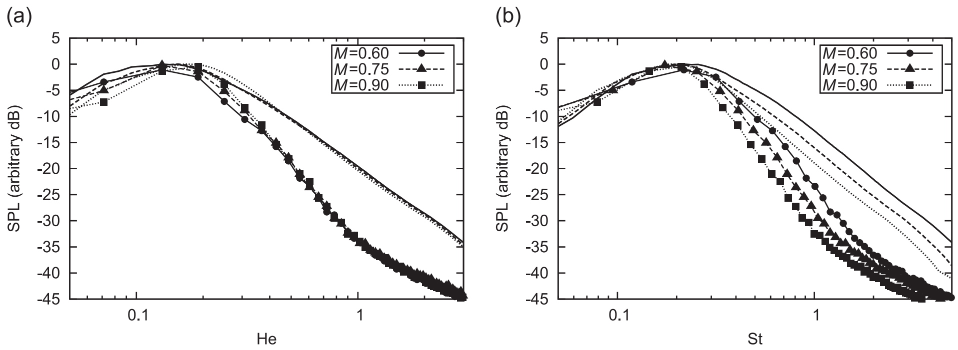

Fig. 14. Spectral shapes at $\theta = 30^{\circ}$ for wavelet CS component of sound field of isothermal jets at different Mach numbers. (a) Spectra scaled by Helmholtz number; (b) spectra scaled by Strouhal number.

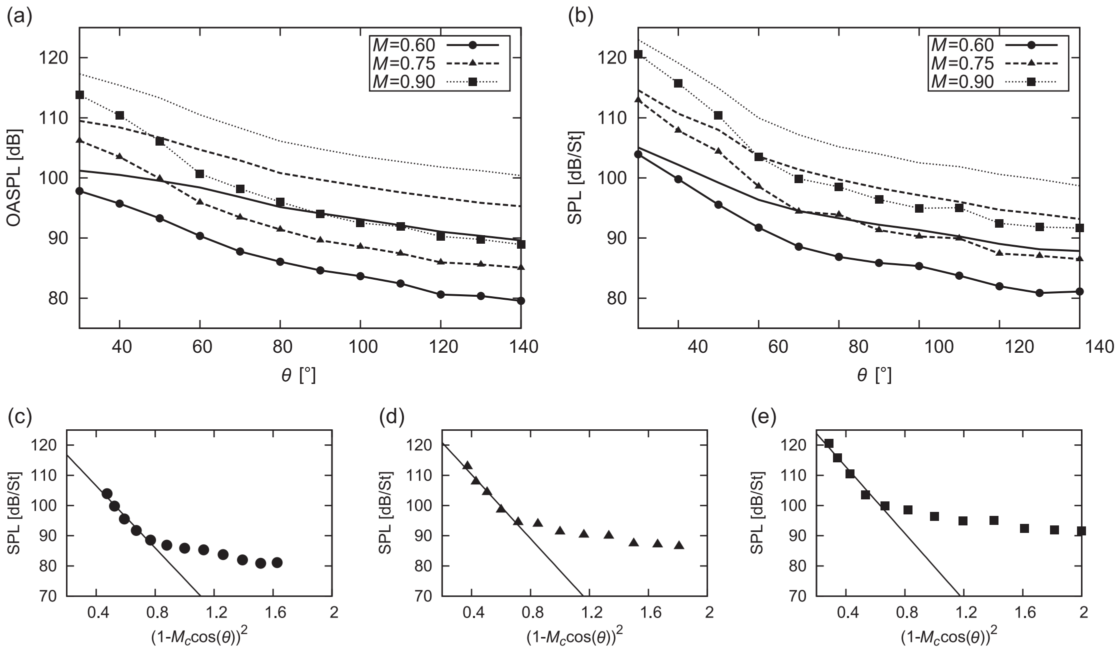

Fig. 15. Directivities for wavelet CS component of sound field of isothermal jets at different Mach numbers. (a) Comparison of OASPL of total sound field and CS component, (b) comparison of SPL, for $St = 0.2$, of total sound field and CS component. Superdirectivity of the CS component for $\alpha = 0.00015$, (c) Mach 0.60, (d) Mach 0.75 and (e) Mach 0.90.

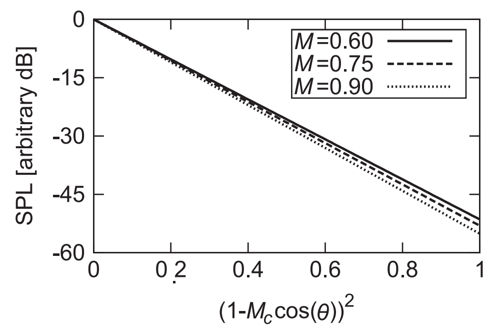

Fig. 16. Comparison of the wavelet CS component superdirectivities for $\alpha = 0.00015$ for the three different Mach numbers.

5.1. Spectra and directivity of unfiltered signals

The spectra are shown in Fig. 17, plotted as a function of both Strouhal and Helmholtz number.

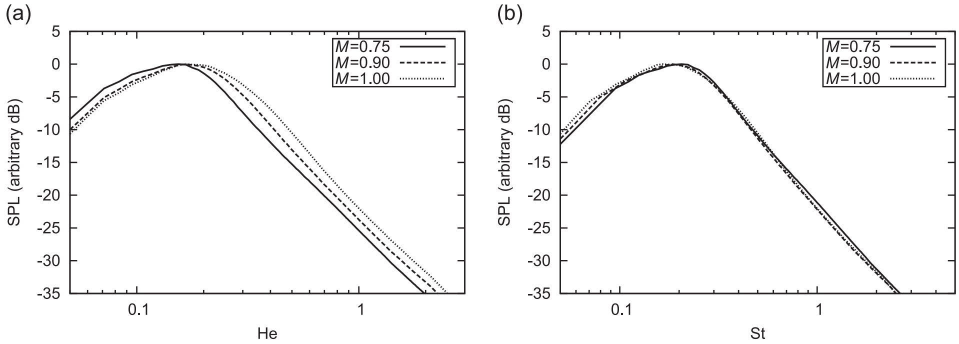

Fig. 17. Spectral shapes for heated jets at different Mach numbers, scaled with (a) Helmholtz and (b) Strouhal numbers at $\theta = 30°$.

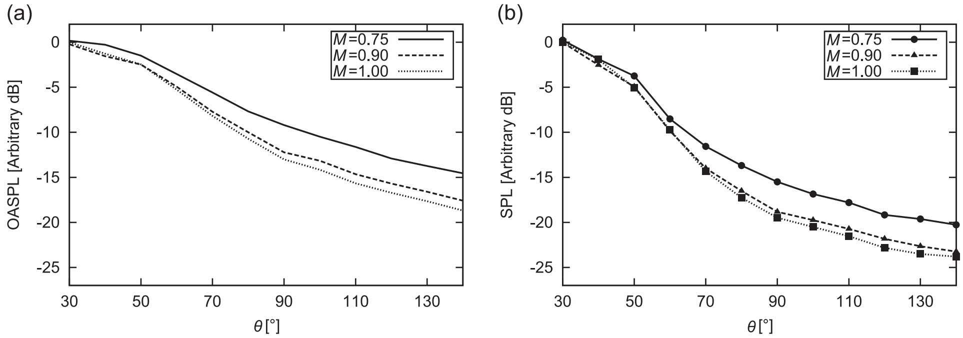

Fig. 18. Directivity of heated jets for different Mach numbers: (a) OASPL; (b) SPL at $St=0.2$.

Contrary to the isothermal case, a better collapse is now obtained when the spectra are plotted as a function the Strouhal number. This suggests that the heated jet is a more compact source than its isothermal counterpart. This compactness may be explained in numerous ways. On one hand, if we consider, once again, the sound source in terms of axially aligned wavepackets, a change in the structural features of the wavepackets could lead to their being more compact in the heated flow; for example the wavepacket envelopes in the hot jet may be shorter than those in the isothermal flow, due for instance to the shortening of the potential core. On the other hand, this difference could be the result of a change in the dispersion relation within the heated part of the flow, on account of the higher sound speed. Of course this region couples with the external medium through which the sound waves generated must propagate, and in the coupling between the two media further attenuation or amplification can occur. These points merit further theoretical and experimental investigation, beyond the scope of this study.

Fig. 18 presents the OASPL directivities of heated jet at different Mach numbers and the SPL value of the spectra at $St=0.2$. The directivities are globally similar to those of the isothermal jets.

5.2. POD filter

The POD CS signatures are evaluated, again, by considering their spectral shapes and directivities. Fig. 19(a) and (b) shows the spectra as a function of both Strouhal and Helmholtz number. The trend observed in the unfiltered result is again preserved: the CS signature also looks to be underpinned by a compact source.

Fig. 20(a) and (b) presents the directivity of the OASPL and the SPL at $St=0.2$ for the CS component; sub figures (c–e) compare these with Crow's wavepacket model, and Fig. 21 summarises the Mach number effect.

5.3. Wavelet filter

The α-curves, shown in Fig. 22 for microphone situated at (a) $\theta = 30°$, (b) $\theta = 40°$ and (c) $\theta = 50°$, indicate that the effect of changing the Mach number of a heated jet is quite different from what is observed in the isothermal case. A clear *decrease* is observed in the temporal jitteriness of the radiated sound, suggesting that an associated change occurs in the source dynamics.

Such ‘jitter’ has been shown by Cavalieri et al. [15] to be a source parameter to which the far field is highly sensitive. This decrease in intermittency with increasing Mach number in heated jets may be related to the fact that at higher Mach

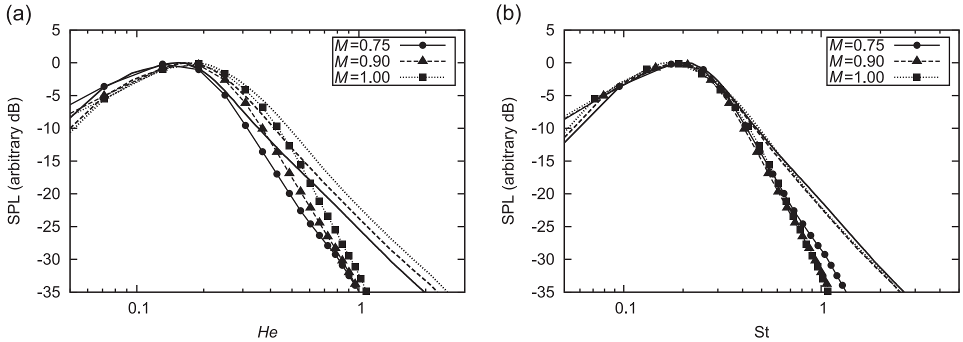

Fig. 19. Spectral shapes at $\theta = 30^\circ$ for POD CS component of sound field of heated jets at different Mach numbers. (a) Spectra scaled by Helmholtz number; (b) spectra scaled by Strouhal number.

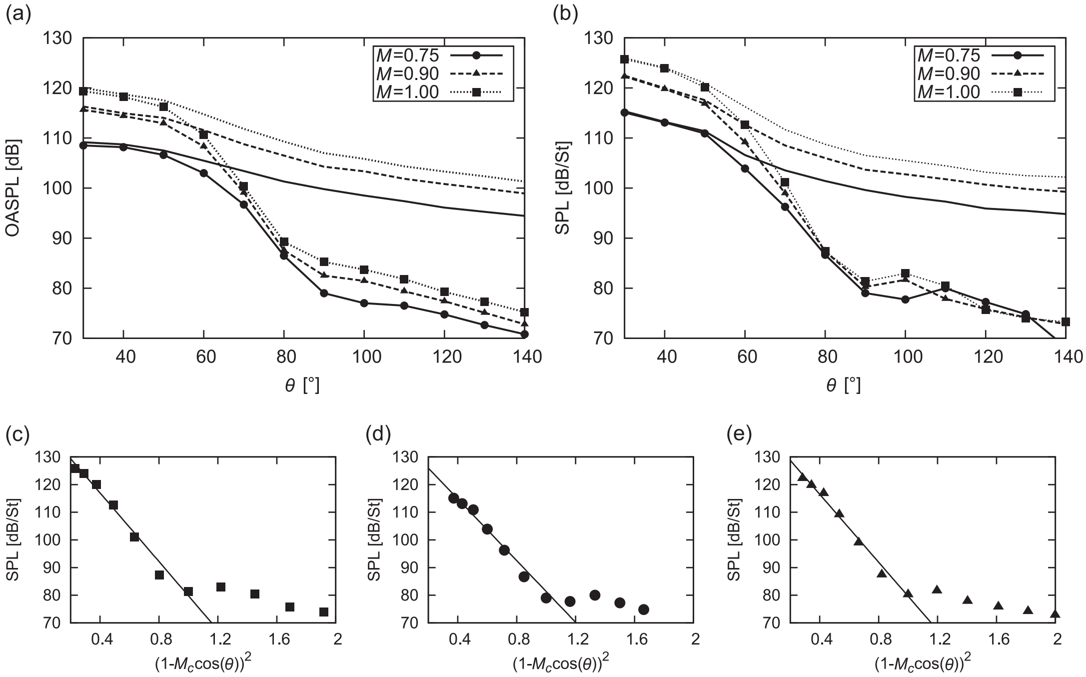

Fig. 20. Directivities for POD CS component of sound field of heated jets at different Mach numbers. (a) Comparison of OASPL of total sound field and CS component; (b) comparison of SPL, for $St = 0.2$, of total sound field and CS component. Superdirectivity of the CS component for (c) Mach 0.75, (d) Mach 0.90 and (e) Mach 1.

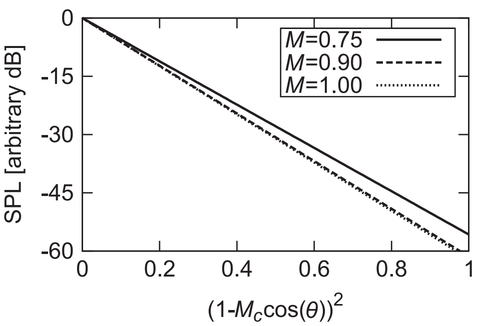

Fig. 21. Comparison of the POD CS component superdirectivities for the three different Mach numbers.

numbers heating a jet reduces its noise. This points merits further exploration but is outside of the scope of the present work.

The wavelet CS spectra are shown in Fig. 23(a) and (b), as a function of Strouhal number and Helmholtz number – the trend of the unfiltered case is again preserved.

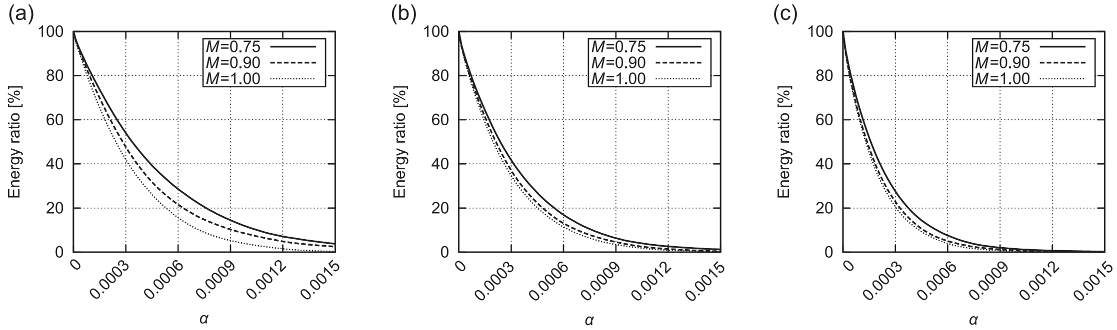

Fig. 22. Energy ratio (filtered/residuum) as a function of Mach number; (a) 30°; (b) 40°; (c) 50°.

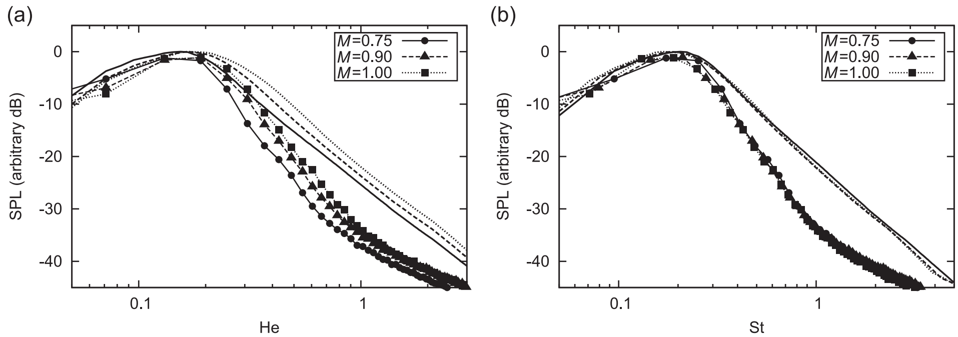

Fig. 23. Spectral shapes at $\theta = 30^{\circ}$ for wavelet CS component of sound field of heated jets at different Mach numbers. (a) Spectra scaled by Helmholtz number; (b) spectra scaled by Strouhal number.

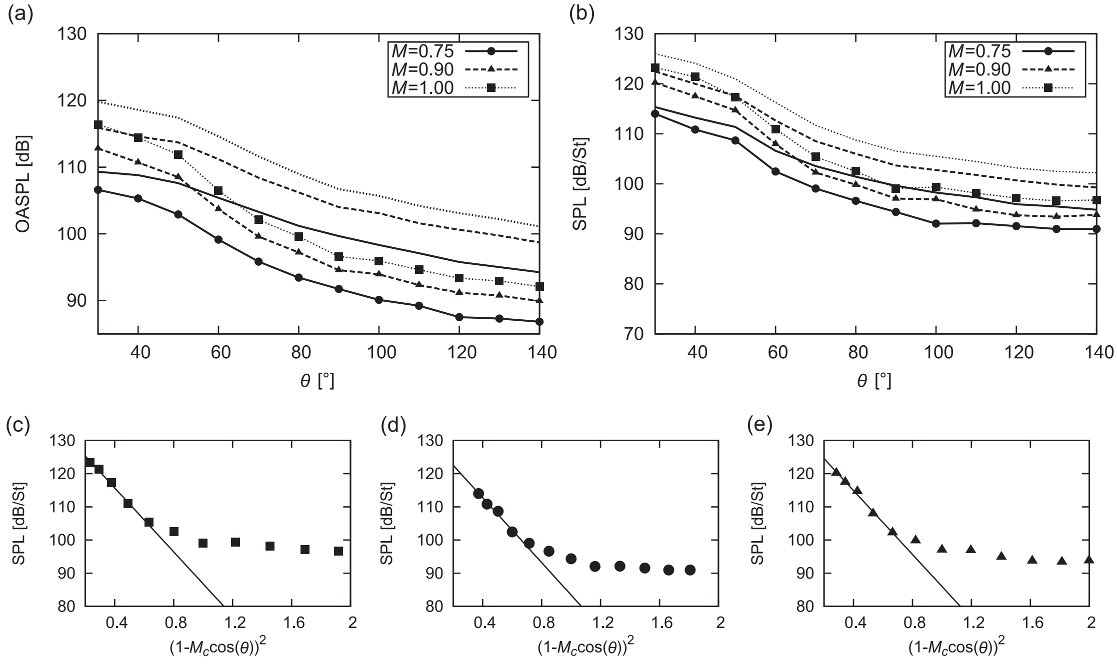

Fig. 24. Directivities for wavelet CS component of sound field of heated jets at different Mach numbers. (a) Comparison of OASPL of total sound field and CS component; (b) comparison of SPL, for $St = 0.2$, of total sound field and CS component. Superdirectivity of the CS component for $\alpha = 0.00015$, (c) Mach 0.75, (d) Mach 0.90 and (e) Mach 1.

The directivity of the wavelet CS component, shown in Fig. 24(c–e), again shows how it may be thought of as synonymous with a wavepacket source. The Mach number effect is summarised in Fig. 25; contrary to the POD result, the Mach number does not impact the directivity so strongly—this is possibly due to the fact that the increased directivity observed in the POD CS signature, a purely spatial trait, is compensated by the decrease in jitter. The directive character of

Please cite this article as: M. Kœnig, et al., Farfield filtering and source imaging of subsonic jet noise, *Journal of Sound and Vibration* (2013), http://dx.doi.org/10.1016/j.jsv.2013.02.040

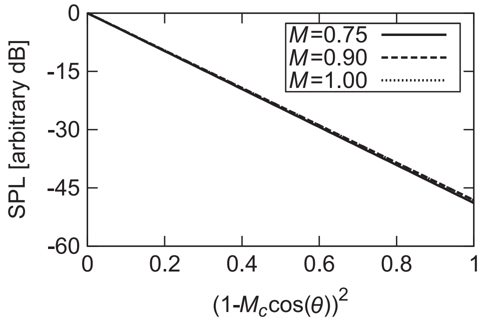

Fig. 25. Comparison of the wavelet CS component superdirectivities for $\alpha = 0.00015$ for the three different Mach numbers.

a wavepacket can be enhanced by a number of source parameters: the convective Mach number, the source compactness and the level of temporal jitter. The POD filter captures the increase in directivity present in the spatial structure of the radiated sound field on account of the increase in kL; whereas the wavelet filter compensates the interference effect with the reduced intermittency effect.

6. Source imaging

In this final section the farfield is explored using a source imaging technique and the results compared with those obtained using the wavelet and POD filters. Such imaging techniques are useful in providing insight regarding source mechanisms (cf. Papamoschou [29] for example), provided: (1) the Ansatz used bears some similarity to the source mechanism; (2) the algorithm converges on a parameter set that is physically realistic. As characteristics consistent with wavepacket radiation were observed in the POD and wavelet CS signatures, a wavepacket Ansatz is used for the imaging procedure.

The general procedure goes as follows. The cross-spectrum $\langle Q(\mathbf{y},\omega)Q^*(\mathbf{y}',\omega)\rangle$ of the sound source field is described in terms of a parameter vector A_k which is determined by "matching" the modelled and measured acoustics. The matching involves the cross-spectral matrix $G(\mathbf{x}_m,\mathbf{x}_n,\omega)$ where $\mathbf{x}_m$ and $\mathbf{x}_n$ denote the spatial locations of measurement points m and n, respectively. The experimental measurement of the CSM is denoted G_{exp}. The modelled CSM is $G_{mod}(\mathbf{A}_k,\mathbf{x}_m,\mathbf{x}_n,\omega)$. It depends on the parameter vector $\mathbf{A}_k$ that describes the source model. Ideally, $\mathbf{A}_k$ would be obtained by setting:

$$G_{exp}(\mathbf{x}_m,\mathbf{x}_n,\omega) = G_{mod}(\mathbf{A}_k,\mathbf{x}_m,\mathbf{x}_n,\omega) \tag{19}$$

and seeking an exact solution for $\mathbf{A}_k$. This is rarely the case however, and so alternative methods must be used that minimise the difference between the modelled and measured acoustic fields. Concentrating on a given frequency ω, the following error function is defined:

$$F(\mathbf{A}_k) = \sum_{m,n=1}^{M} |G_{exp}(\mathbf{x}_m,\mathbf{x}_n) - G_{mod}(\mathbf{A}_k,\mathbf{x}_m,\mathbf{x}_n)|^2, \tag{20}$$

where M is the total number of measuring stations. A vector $\mathbf{A}_k$ is sought that minimises $F(\mathbf{A}_k)$. A method that has proven effective is the conjugate gradient minimisation method, particularly as implemented by Shanno and Phua [30].

To calculate the modelled CSM, a cylindrical surface of radius $r = r_0$ is considered (we take the jet radius as r_0 in our case). Analytical solution for the sound radiation from a cylindrical surface is reported in Morse and Ingard [31]. The pressure on the cylindrical surface is then prescribed as

$$p(r_0,x,t) = p_0(x,\mathbf{A}_k)\mathrm{e}^{-\mathrm{i}\omega t} \tag{21}$$

where $p_0(x,A_k)$ takes the form of a wavepacket that amplifies and decays with x and is axisymmetric. For a given frequency ω and radius R, the modelled CSM is (see for instance Freund's appendix [32] or Morris [33]):

$$G_{mod}(\mathbf{A}_k,\theta_m,\theta_n) = \frac{1}{\pi R^2}\frac{\hat{p}_0\left(\frac{\omega}{c_\infty}\cos\theta_m,\mathbf{A}_k\right)\hat{p}_0^*\left(\frac{\omega}{c_\infty}\cos\theta_n,\mathbf{A}_k\right)}{H_0^{(1)}\left(\frac{\omega}{c_\infty}r_0\sin\theta_m\right)H_0^{(2)}\left(\frac{\omega}{c_\infty}r_0\sin\theta_n\right)}, \tag{22}$$

where $\hat{p}_0$ is the wavenumber transform of p_0. More details about this procedure and the calculation of the modelled CSM can be found in Papamoschou [34,4].

Fig. 26 illustrates how the modelled CSM has been fitted with the measured CSM for a Mach 0.9 cold jet at $St = 0.15$ with a wavepacket *Ansatz* presented below. The fitting process is applied using the entire cross-spectral matrix. A satisfactory agreement is obtained for low angles.

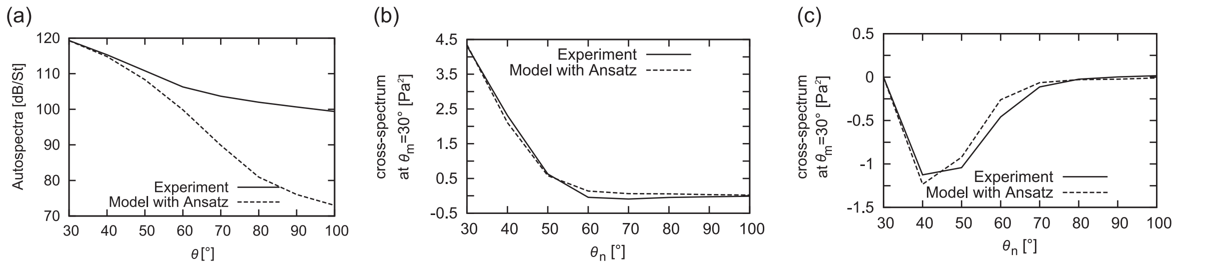

Fig. 26. Comparison between modelled CSM and measured CSM for a Mach 0.9 cold jet at $St=0.15$. (a) Autospectrum; (b) real part of cross-spectrum at 30°; (c) imaginary part of cross-spectrum at 30°.

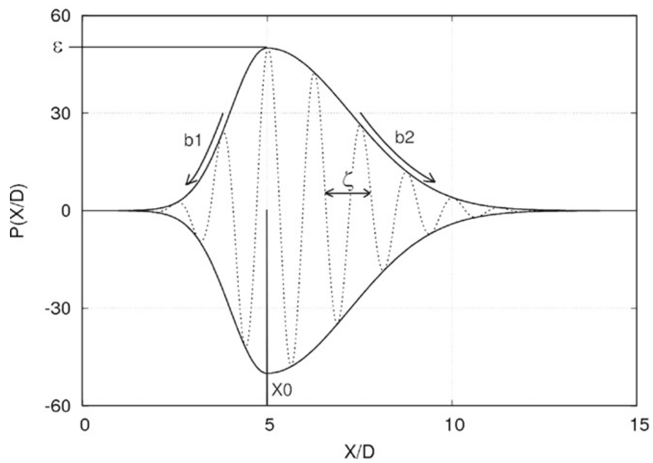

Fig. 27. Asymmetric Gaussian curve used for the wavepacket model.

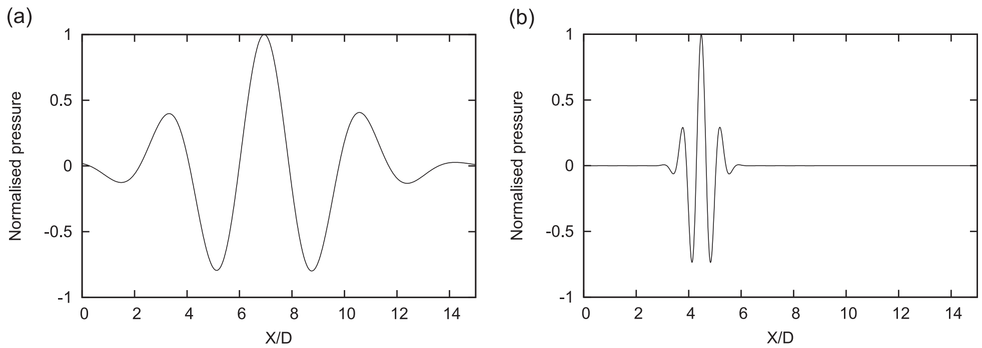

Fig. 28. Source distributions obtained for a Mach 0.9 cold jet at (a) $St=0.15$ and (b) $St=0.5$.

In addition, we here consider only low frequencies ($St=0.05$ to $St=0.5$). Cavalieri et al. [24] show that in this frequency range, for low-angle radiation, the axisymmetric mode dominates. The wavepacket Ansatz is thus valid for the frequencies considered.

Asymmetric wavepacket Ansatz. The axial structure of the Ansatz comprises an eventual asymmetry:

$$p_0(x,\mathbf{A}_k) = \epsilon B(x) \mathrm{e}^{\mathrm{i}\zeta x}, \tag{23}$$

where is $B(x)$ is the piecewise-defined function:

$$B(x) = \begin{cases} \exp(-b_1(x-x_0)^2), & x \leq x_0 \\ \exp(-b_2(x-x_0)^2), & x > x_0 \end{cases}. \tag{24}$$

The vector $\mathbf{A}_k$ is composed of five parameters (ϵ, ζ, b_1, b_2, x_0) as shown in Fig. 27. A similar Ansatz was previously used by Papamoschou [34] to predict jet noise shielding. In our case, the axial parameter is normalised by the jet diameter.

An analytical expression for $\hat{p}_0(k,\mathbf{A}_k)$ is

$$\hat{p}_0(k,\mathbf{A}_k) = \frac{\epsilon\sqrt{\pi}}{2}\,\mathrm{e}^{\mathrm{i}x_0(k-\zeta)}\left(\frac{1}{\sqrt{b_2}}W(\beta_2)+\frac{1}{\sqrt{b_1}}W^*(\beta_1)\right), \tag{25}$$

with $\beta_1=(k-\zeta)/\sqrt{b_1}$, $\beta_2=(k-\zeta)\sqrt{b_2}$ and $W(x)=\mathrm{e}^{-x^2}\,\mathrm{erfc}(\mathrm{i}x)$ the Faddeeva function.

An example of the source distributions obtained for a Mach 0.9 cold jet at $St=0.15$ and $St=0.50$ is shown in Fig. 28. As expected, at low Strouhal numbers the source extent (which can be linked to the slopes values b_1 and b_2 in Eq. (24)) is large. When the Strouhal number is increased, the source distribution is closer to the nozzle exit and more localised.

The effect of Mach number on these parameters, for both isothermal and heated jets, is now explored.

6.1. Mach number dependence of wavepacket parameters for isothermal jet

Cases 1–3 are considered (see Table 1). Fig. 29 presents the results, and compares the directivities with those of the POD and wavelet CS signatures.

The main trends observed, as the Mach number is increased, comprise a displacement of the wavepacket in the downstream direction. The wavepacket center position is found to lie around five or six diameters from the jet exit at $St=0.2$ which is in fair agreement with other studies [35,9] even if positions at low frequencies seem a little exaggerated. A slight decrease of the convection velocity is also observed; this is consistent with the trend predicted by linear stability theory [36], even if the absolute values are a little lower than expected.

Fig. 29(c)–(e) compared the directivity obtained using the imaging technique with the POD and wavelet CS directivities. Close agreement is observed at low emission angles. This close agreement is again a strong evidence to support the contention that wavepackets drive the downstream radiation, and that their superdirective radiation is underpinned both by their axial wavelike structure and their temporal jitter. The $(1-M_c\cos(\theta))^2$ trend remains relevant as the parameters identified by the algorithm indicate a symmetric envelope, as can be seen in Fig. 30.

6.2. Mach number dependence of wavepacket parameters for heated jet

The heated jet is now considered: cases 4–6 in Table 1. Fig. 31 summarises the results.

Similar Mach number effects are observed: the wavepacket position moves downstream with increasing Mach number, again consistent with the associated lengthening of the potential core, and a slight decrease of the convection velocity, consistent with the trend predicted by linear stability theory.

The directivity of the wavepacket source identified is again superdirective, and agrees favourably with the POD and wavelet CS signatures. This superdirective behaviour corresponds well to the superdirective behaviour previously identified after the POD or the wavelet filtering operation.

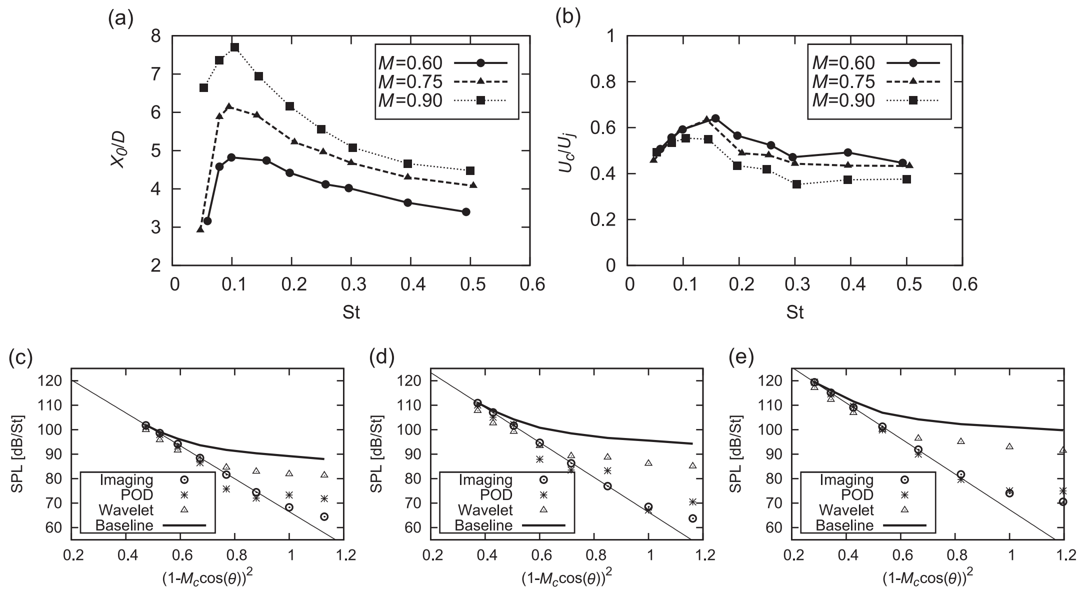

Fig. 29. Wavepacket parameters, for isothermal jet, as a function of Strouhal and Mach number. (a) wavepacket center; (b) convection velocity. Wavepacket superdirectivity: (c), (d) and (e) correspond to Mach 0.6, 0.75 and 0.9, respectively. Results in (c), (d) and (e) are presented at $St=0.21$.

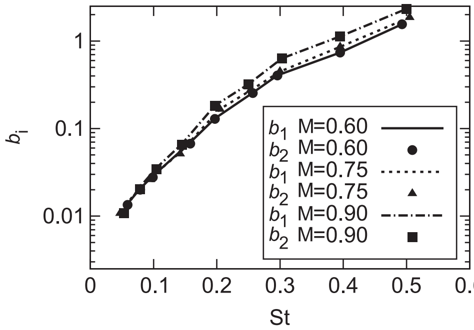

Fig. 30. Wavepacket slopes, for isothermal jet, as a function of Strouhal and Mach number.

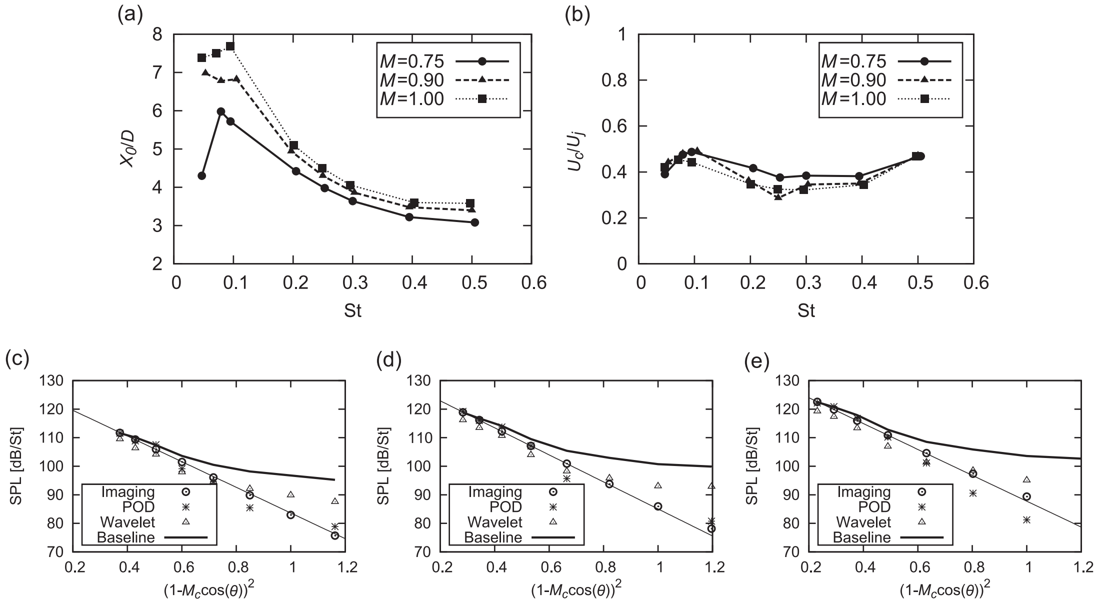

Fig. 31. Wavepacket parameters, for heated jet, as a function of Strouhal and Mach number. (a) Wavepacket center; (b) convection velocity. Wavepacket superdirectivity: (c), (d) & (e) correspond to Mach 0.75, 0.9 and 1, respectively. Results in (c), (d) and (e) are presented at $St=0.21$.

7. Conclusions

An analysis methodology, tailored to probe jet noise in ways that are not possible using Fourier analysis, is presented and applied to a jet noise database. Proper Orthogonal Decomposition and wavelet transforms are used to interrogate the spatial (polar) and temporal structures of the sound field: metrics associated with these 'directions' of the farfield are established and used to educe the signature of coherent structures (CS).

The methodology is then used to explore the effect of Mach number on jet noise in isothermal and heated jets. The main results obtained from this phase of the analysis are the following: (1) filters based on both the polar and temporal structures isolate a CS signature consistent with a wavepacket source; (2) consistent with the unfiltered spectra, both the POD and wavelet CS spectra scale with Helmboltz number in isothermal jets, whereas they scale with Strouhal number in the heated jets; this suggests that wavepackets in isothermal jets are noncompact, whereas in heated jets they are compact; (3) while increasing the Mach number of an isothermal jet has no significant effect on the intermittency of the low-angle sound emission, increasing the Mach number of a heated jet leads to a decrease in that intermittency, hinting at some kind of associated stabilising of wavepacket source dynamics.

Finally, application of a source imaging algorithm allows the dependence of the wavepacket parameters on Mach number and temperature to be assessed. The results show how increasing the Mach number causes wavepacket sources to move downstream, and leads to a slight reduction in their convection velocity (consistent with predictions of linear stability theory). Comparison of the directivity of the source wavepackets obtained by the imaging with those educed from the data using the aforesaid filtering operations shows good agreement: this result constitutes evidence that wavepackets are an essential element underpinning sound radiation to low polar angles, and that the salient wavepacket parameters are their axial waviness, their convection velocities and their temporal jitter. At larger polar angles the axisymmetric wavepacket is not found to make significant contributions to the radiated sound. This is expected. Exploration of the source characteristics associated with this component of the sound radiation would require the use of a more complete source model, and azimuthal microphone arrays which permit analysis of the polar structure of the higher-order azimuthal modes known to dominate radiation to higher polar angles [23,24].

Acknowledgments

The present work was initiated during the 3rd IFFC held in Poitiers in 2008. It was supported by SNECMA (Safran Group) and CNPq, National Council of Scientific and Technological Development – Brazil.

Appendix A. Evaluation of real- and complex-valued wavelets

In this paper, we deal with real-valued pressure signals. However, we chose to use complex-valued wavelets to perform the wavelet filtering operation. The motivation for using such a wavelet is that it better preserves the integrity of something which can be associated with a single "event", on account of that fact that the real and imaginary parts of the wavelet allow both high energy peaks and zero crossings associated with a given signature to contribute continually over an integral scale over which the event is active. Real wavelets will tend to break such single events into unphysical sub-events. Fig. A1 shows the effect of a filter with real- (Mexican hat) and complex-valued (Paul) wavelets. When three events are identified by the real-valued wavelet in the pressure scalogram, only one event is retained by a Paul wavelet. This is due to the fact that

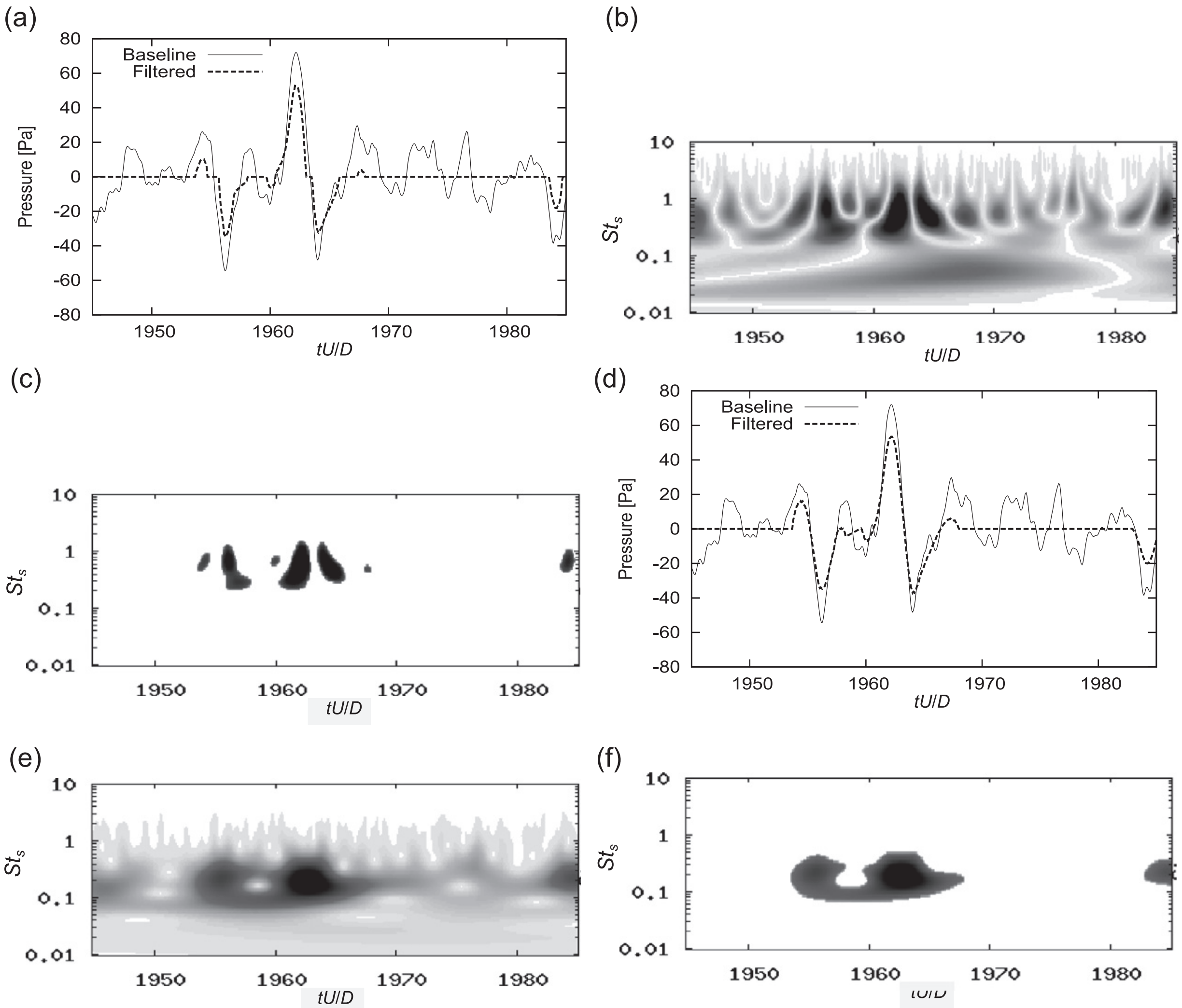

Fig. A1. Top: temporal filtered signals by a (a) real- and (d) complex-valued wavelet. Middle: Original scalograms obtained with a (b) real- and (e) complex-valued wavelet. Bottom: Filtered scalograms obtained with a (c) real- and (f) complex-valued wavelet. (see Fig. 4 for colour scale).

real-wavelets will lead to zero energy in the wavelet domain when convolved with zero-crossing in the pressure signal as highlighted in the bottom figures of Fig. A1.

Appendix B. Impact of the mother wavelet choice

We show that the conclusions obtained using the wavelet filter are insensitive to the choice of mother wavelet by investigating three kinds of mother wavelets defined as (Fig. B1)

$$\text{Mexican hat (real)}: \ \psi(t) = \frac{(-1)^{m+1}}{\sqrt{\Gamma(m+\frac{1}{2})}} \frac{d^m}{d\eta^m}(e^{-\eta^2/2}) \tag{B.1}$$

$$\text{Morlet (complex)}: \ \psi(t) = \pi^{-1/4} e^{i\omega_0 \eta} e^{-\eta^2/2} \tag{B.2}$$

$$\text{Paul (complex)}: \ \psi(t) = \frac{2^m i^m m!}{\sqrt{\pi(2m)!}}(1-i\eta)^{-(m+1)} \tag{B.3}$$

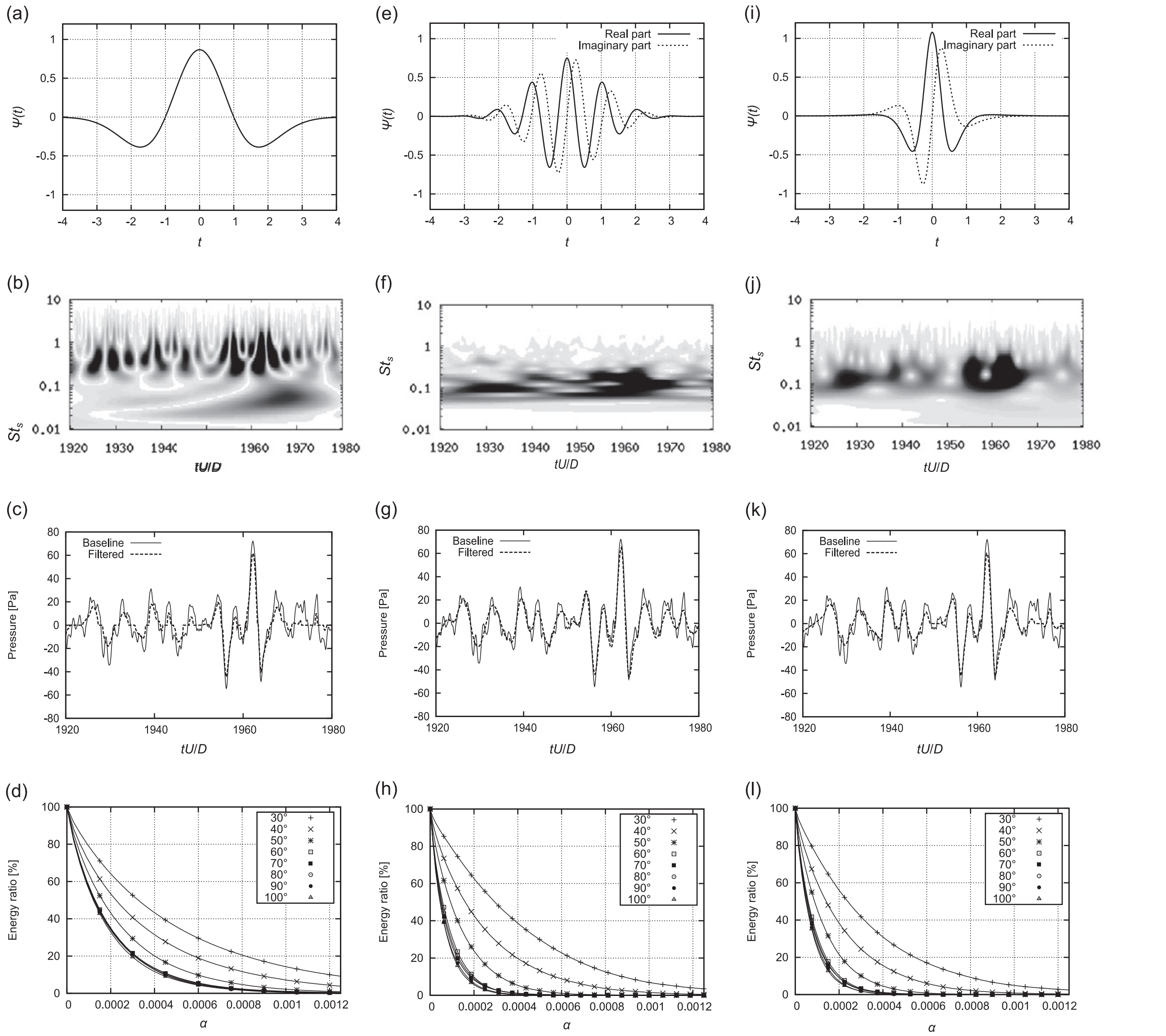

Fig. B1. Wavelet comparisons by: mother wavelets (a) Mexican hat, (e) Morlet, (i) Paul; scalograms (b) Mexican hat, (f) Morlet, (j) Paul (see Fig. 4 for colour scale); temporal filtered signals (c) Mexican hat, (g) Morlet, (k) Paul; energy ratio (d) Mexican hat, (h) Morlet, and (l) Paul.

Please cite this article as: M. Kœnig, et al., Farfield filtering and source imaging of subsonic jet noise, *Journal of Sound and Vibration* (2013), http://dx.doi.org/10.1016/j.jsv.2013.02.040

References

[1] H.K. Tanna, An experimental study of jet noise Part I: *turbulent mixing noise*, *Journal of Sound and Vibration* 50 (3) (1977) 405–428.
[2] E. Mollo-Christensen, Jet noise and shear flow instability seen from an experimenter's viewpoint (similarity laws for jet noise and shear flow instability as suggested by experiments), *Journal of Applied Mechanics* 34 (1967) 1–7.
[3] C.K.W. Tam, M. Golebiowski, J.M. Seiner, On the two components of turbulent mixing noise from supersonic jets, *2nd AIAA/CEAS Aeroacoustics Conference* (*17th AIAA Aeroacoustics Conference*), 1996, pp. 96–1716.
[4] D. Papamoschou, Wavepacket modeling of the jet noise source, *17th AIAA/CEAS Aeroacoustics Conference* (*32nd AIAA Aeroacoustics Conference*), 2011.
[5] A. Michalke, Instabilität eines Kompressiblen Runden Freistrahls unter Berücksichtigung des Einflusses der Strahlgrenzschichtdicke (instability of a compressible circular free jet with consideration of the influence of jet boundary layer thickness), Zeitschrift Flugwiss, English translation: NASA TM 75190, 1977 19 (1971) 311–328.
[6] D.G. Crighton, M. Gaster, Stability of slowly diverging jet flow, *Journal of Fluid Mechanics* 77 (2) (1976) 397–413.
[7] K. Gudmundsson, T. Colonius, Instability-wave models for the near field fluctuations of turbulent jets, *Journal of Fluid Mechanics* 689 (2011) 97–128.
[8] P. Jordan, Jet Noise Control, Flow Control: Fundamentals, Advances and Applications, *Von Karman Institute Lecture series*, March 2009.
[9] D. Juvé, M. Sunyach, G. Comte-Bellot, Intermittency of the noise emission in subsonic cold jets, *Journal of Sound and Vibration* 71 (1980) 319–332.
[10] G. Guj, R. Carley, C. Camussi, Acoustic identification of coherent structures in a turbulent jet, *Journal of Sound and Vibration* 259 (2003) 1037–1065.
[11] J.I. Hileman, B.S. Thurow, E.J. Carabello, M. Samimy, Large-scale structure evolution and sound emission in high-speed jets: real-time visualisation with simultaneous acoustic measurements, *Journal of Fluid Mechanics* 544 (2005) 277–307.
[12] A.V.G. Cavalieri, P. Jordan, Y. Gervais, M. Wei, J.B. Freund, Intermittent sound generation and its control in a free-shear flow, *Physics of Fluids* 22 (2010).
[13] D. Grassucci, P. Jordan, R. Camussi, Combined wavelet and linear stochastic estimation analysis, *16th AIAA/CEAS Aeroacoustics Conference* (*31st AIAA Aeroacoustics Conference*), 2010.
[14] N. Sandham, C. Morfey, Z. Hu, Sound radiation from exponentially growing and decaying waves, *Journal of Sound and Vibration* 294 (2006) 355–361.
[15] A.V.G. Cavalieri, P. Jordan, A. Agarwal, Y. Gervais, Jittering wave-packet models for subsonic jet noise, *Journal of Sound and Vibration* 330 (18) (2011) 4474–4492.
[16] S.C. Crow, *Acoustic Gain of a Turbulent Jet, in Physical Society Meeting*, University of Colorado, Boulder, 1972.
[17] P. Jordan, Y. Gervais, Modelling self- and shear-noise mechanisms in inhomogeneous, anisotropic turbulence, *Journal of Sound and Vibration* 279 (2005) 529–555.
[18] J. Delville, L. Ukeiley, L. Cordier, J.P. Bonnet, M. Glauser, Examination of large-scale structures in a turbulent plane mixing layer. Part 1. Proper orthogonal decomposition, *Journal of Fluid Mechanics* 391 (1999) 91–122.
[19] C.E. Tinney, P. Jordan, The near pressure field of co-axial subsonic jets, *Journal of Fluid Mechanics* 611 (2008) 175–204.
[20] D.G. Crighton, Basic principles of aerodynamic noise generation, *Progress in Aerospace Sciences* 16 (1975) 31–96.
[21] J.E. Ffowcs Williams, A.J. Kempton, The noise from the large-scale structure of a jet, *Journal of Fluid Mechanics* 84 (1978) 673–694.
[22] D.G. Crighton, P. Huerre, Shear layer pressure fluctuations and superdirective acoustic sources, *Journal of Fluid Mechanics* 220 (1990) 355–368.
[23] D. Juvé, M. Sunyach, G. Comte-Bellot, Filtered azimuthal correlations in the acoustic far field of a subsonic jet, *AIAA Journal* 17 (1979) 112–113.
[24] A.V.G. Cavalieri, P. Jordan, T. Colonius, Y. Gervais, Axisymmetric superdirectivity in subsonic jets, *Journal of Fluid Mechanics* 704 (2012) 388–420.
[25] M. Farge, Wavelet transforms and their applications to turbulence, *Annual Review of Fluid Mechanics* 24 (1992) 395–458.
[26] C. Torrence, G. Compo, A practical guide to wavelet analysis, *Bulletin of the American Meteorological Society* 79 (1) (1998) 61–78.
[27] P.A. Lush, Measurements of subsonic jet noise and comparison with theory, *Journal of Fluid Mechanics* 46 (3) (1971) 477–500.
[28] K. Viswanathan, Aeroacoustics of hot jets, *Journal of Fluid Mechanics* 516 (2004) 39–82.
[29] D. Papamoschou, Imaging of directional distributed noise sources, *Journal of Sound and Vibration* 330 (10) (2010) 2265–2280.
[30] D.F. Shanno, K.H. Phua, Minimization of unconstrained multivariate functions, *ACM Transactions on Mathematical Software* 6 (4) (1980) 618–622.
[31] P.M.C. Morse, K.U. Ingard, *Theoretical Acoustics*, Princeton University Press, 1968.
[32] J.B. Freund, Noise sources in a low-Reynolds-number turbulent jet at Mach 0.9, *Journal of Fluid Mechanics* 438 (2001) 277–305.
[33] P.J. Morris, A note on noise generation by large scale turbulent structures in subsonic and supersonic jets, *International Journal of Aeroacoustics* 8 (4) (2009) 301–315.
[34] D. Papamoschou, Prediction of jet noise shielding, *48th AIAA Aerospace Sciences Meeting*, 2010.
[35] W.T. Chu, R.E. Kaplan, Use of a spherical concave reflector for jet-noise-source distribution diagnosis, *The Journal of the Acoustical Society of America* 59 (1976) 1268–1277.
[36] A. Michalke, Survey on jet instability theory, *Progress in Aerospace Sciences* 21 (1984) 159–199.

Please cite this article as: M. Kœnig, et al., Farfield filtering and source imaging of subsonic jet noise, *Journal of Sound and Vibration* (2013), http://dx.doi.org/10.1016/j.jsv.2013.02.040